國立臺灣大學理學院物理學系

博士論文

Department of Physics

College of Science

National Taiwan University

Doctoral Dissertation

分子與金屬介面的組態與磁性之第一原理研究

First-principles study on the configurations and magnetic properties of molecules and metal interfaces

彭冠瑋

Guan-Wei Peng

指導教授: 關肇正 博士

張允崇 博士

Advisor: Chao-Cheng Kaun, Ph.D.

Yun-Chorng Chang, Ph.D.

中華民國 113 年 10 月

October 2024

doi:doi:10.6342/NTU202404801

Acknowledgements

在台灣大學攻讀博士學位期間，我最感謝家母和家姊一直以來的支持，博士學位花費比預期還久，在家人的幫助和鼓勵下，我才能完成這個學位。感謝擔任口試委員的張允崇教授、張景皓教授、蔡政達教授、郭錦龍教授以及薛宏中教授對研究及論文的討論、建議和指教。特別感謝共同指導的張允崇教授的幫助。

博士階段的研究很感謝指導教授關肇正老師的指導，在研究的題目以及研究方向上老師提供的莫大的協助，研究期間老師也對學生我循循善善，碰到問題都能給予我及時的建議與提點，更提供非常完善的研究資源，除了團隊在中研院有伺服器以外，也能使用師大和國家高速網路與計算中心的台灣杉雲端伺服器，特別是國高的台灣杉提供強大的計算能力和足夠多的記憶體，研究的計算才能順利推展。在此也感謝同組團隊林冠伯學長、蔡晴羽同學、余宜馨同學等夥伴在期間的討論與協助。

巨磁阻系統的研究和張景皓教授的團隊合作，感謝張景皓老師的建議與指導，宏晉的解析計算和研究建議，雨潔學姊在文章的建議和寫作上的指導、協助。在鉍銅表面合金研究，感謝合作的徐斌睿教授的團隊提供實驗上的資料和研究建議。

泛函密度理論我在碩士研究時一直是只聞其名，沒有深入了解過，特別感謝國家理論科學研究中心開設「第一原理材料計算課程」，這課程讓學生快速了解第

doi:doi:10.6342/NTU202404801

一原理理論背景，以及軟體 (特別是 VASP) 使用方式。也感謝郭光宇老師在我博士班前期的指導，讓我對第一原理計算建立良好的研究基礎，也感謝那段時間詹勳奇學長、劉承祐學長和王子政同學等同組成員的幫助。還要感謝蔡政達教授在所上教授的泛函密度理論課程，讓我對理論能有更清楚了解。

doi:doi:10.6342/NTU202404801

摘要

這篇論文使用基於泛含密度理論的第一原理計算分子與金屬材料介面或金屬與金屬介面間的物理性質，特別著重在不同磁性組態的行為，旨在了解一些特殊物理性質背後的物理原理。文章研究的系統有三種：1. 由兩層磁性金屬夾著一層非磁性金屬構成的巨磁阻系統；2. 將銅沉積在鉍表面形成的合金；3. 具有手性的胜肽（peptide）分子在帶磁性的鈷鍍金表面的吸附力研究。

早期的巨磁阻系統研究發現，該系統兩側金屬的磁性方向可能不是整齊的相互平行或相互反平行，而是帶有部分垂直分量。為此，我們計算了不同厚度的中間非磁性金屬層的層間交換耦合（interlayer exchange coupling），以了解兩側磁性金屬磁矩方向選擇的特性。此外，在兩側磁矩相互垂直的系統中，我們發現了成對出現的特殊能帶，這些能帶在實空間的磁矩沿垂直介面方向呈現順時針方向和逆時針方向旋轉。

實驗發現，銅在鉍表面沉積後形成的二銅一鉍（$BiCu_2$）合金，在施加特定偏壓时，该合金的電導會突然大幅上升。我們嘗試通過第一原理計算此系統的能帶結構及態密度，以材料的物理性質從理論上理解電導大幅上升的原因。

實驗測量了具有手性的胜肽分子在磁性表面的吸附力，發現不同磁性方向（進表面或出表面）之間存在相當強度的差距。利用第一原理計算，我們計算此系統的能量，試圖探討吸附力差距的來源及其物理機制。

doi:doi:10.6342/NTU202404801

關鍵字：第一原理、磁矩、層間交換耦合、非共線排列、巨磁阻系統、拉什巴效應、手性誘導自旋選擇性

doi:doi:10.6342/NTU202404801

Abstract

This dissertation employed first-principles calculations to study molecule-metal and metal-metal interfaces, with a particular focus on their configurations and magnetic properties. The objective was to elucidate the physical mechanisms underlying unusual phenomena. Three systems are studied in this research: 1. a giant magnetoresistive system consisting of two layers of magnetic metal sandwiching a non-magnetic metal spacer; 2. an alloy formed by depositing Cu on a Bi surface; and 3. the adsorption of a chiral peptide molecule on Au/Co surfaces with magnetic moment.

Initial studies of the giant magnetoresistive system indicated that the direction of metallic magnetism in both side layers may not be perfectly parallel or antiparallel, but may have a partially perpendicular component. To address this, we calculate the interlayer exchange coupling (IEC) of the system with different thicknesses of the non-magnetic spacer to improve our understanding of its properties concerning the orientations of the magnetic moments on both sides. Furthermore, in configurations where the magnetic mo-

doi:doi:10.6342/NTU202404801

ments are perpendicular to each other, we observed a pair of stripes of magnetic moments rotating clockwise and counterclockwise in real space along a direction perpendicular to the interface.

The deposition of Cu on the Bi surface results in the formation of the $BiCu_2$ alloy, which exhibits a sudden and significant increase in conductivity at a specific bias voltage. To comprehend the underlying physical mechanism responsible for this dramatic increase in conductivity, we have calculated the band structure and density of states of this system from first principles.

The adsorption of chiral molecules on magnetic surfaces was measured and the results showed significant differences in magnetic orientation attraction (in-plane vs. out-of-plane). To understand the physics behind this difference, we performed ab initio calculations to determine the energy of the system.

Keywords: first-principles, magnetic moment, interlayer exchange coupling, noncollinear alignment, metallic trilayer, Rashiba effect, Chirality-induced spin selectivity (CISS)

doi:doi:10.6342/NTU202404801

Contents

doi:doi:10.6342/NTU202404801

doi:doi:10.6342/NTU202404801

List of Figures

doi:doi:10.6342/NTU202404801

doi:doi:10.6342/NTU202404801

doi:doi:10.6342/NTU202404801

doi:doi:10.6342/NTU202404801

List of Tables

doi:doi:10.6342/NTU202404801

doi:doi:10.6342/NTU202404801

Chapter 1 Introduction

As technology advances, the fabrication of nanoscale devices is becoming increasingly feasible. The interfacial properties and quantum effects of the nanoscale devices are critical in determining their physical properties. First-principles calculations can be effectively applied at this scale range. By analyzing the band structure and density of states, the electrical and magnetic properties of the device can be fully understood. In this dissertation, three systems with magnetic moments and interfaces are studied, and the experimentally observed phenomena are elucidated using first-principles calculations.

The first-principles calculations discussed in this dissertation were based on density functional theory (DFT). Chapter 2 provides a brief overview of DFT. The calculations presented in this dissertation were performed using the Vienna Ab initio Simulation Package (VASP). [1–4]

Chapter 3 considers a giant magnetoresistive system consisting of two magnetic metal layers sandwiching a non-magnetic metal spacer. Recent experiments on Co/Ir/Co and Co/Ru/Co trilayers have shown that manipulating the width or properties of the spacer layer can induce noncollinear and even perpendicular magnetic alignment between the Co layers. Using first-principles methods to investigate the interlayer exchange coupling (IEC) in the Fe/Ag/Fe trilayer, we find that the magnetic moments of the two Fe layers tend

doi:doi:10.6342/NTU202404801

to align perpendicularly for a given width of the Ag layer. Our results are in agreement with the analytical calculations performed by a collaborator. [5] We have also found a relationship between the IEC and the magnetic orientation of the system. In particular, unique bands emerge in pairs, and the magnetic moments within these bands show a spiral rotation across the trilayer. These results demonstrate that nonlinear IEC provides a certain degree of freedom in controlling magnetic configuration, thereby increasing the load carrying capacity of spintronics technology.

Cu deposition on the Bi surface results in of the alloy, BiCu2, which is discussed in Chapter 4. Under certain voltage conditions, the conductivity of this system increases significantly. We employed first-principles methods to calculate the band structure and density of states for 2 to 8 layers of Bi. However, the projected band structures do not agree well with the previous Korringa-Kohn-Rostoker (KKR) calculations. [6] Nevertheless, I have gained considerable knowledge in this area.

The adsorption forces of chiral peptides on an Au/Co surface were measured, revealing significant differences in the direction of the surface magnetic moment. [7] In Chapter 5, the total energy of chiral peptides on the Au/Co surface is investigated. However, the results do not correlate well with the experimental data, and the reasons for this discrepancy are discussed.

doi:doi:10.6342/NTU202404801

Chapter 2 Method

2.1 Density Functional Theory

In solid state physics, the systems of interest typically consist of many atoms within a repeating unit cell. Consequently, the challenge is to solve the time-independent many-body Schrödinger equation. [8]

$$\hat{H}\psi(\{\vec{r}_i\},\{\vec{R}_a\}) = E\psi(\{\vec{r}_i\},\{\vec{R}_a\}) \tag{2.1}$$

$$\begin{aligned}\hat{H} = & \sum_{a=1}^{M}\frac{-\hbar^2}{2M_a}\nabla_a^2 + \sum_{a=1}^{M-1}\sum_{b=a+1}^{M}\frac{Z_a Z_b e^2}{R_{ab}} && (\hat{H}_{nucleus}) \\ & + \sum_{i=1}^{N}\frac{-\hbar^2}{2M_e}\nabla_i^2 + \sum_{i=1}^{N-1}\sum_{j=i+1}^{N}\frac{e^2}{r_{ij}} && (\hat{H}_{electron}) \\ & - \sum_{a=1}^{M}\sum_{i=1}^{N}\frac{Z_a e^2}{r_{ai}} && (\hat{H}_{electron-nucleus}) \\ & + V(\{r_i\},\{R_a\}) \end{aligned} \tag{2.2}$$

where, $\vec{r}_i$ is the position vector for the i-th electron, $\vec{R}_a$ is the position vector for the a-th nucleus, r_{ai} is the distance between the a-th nucleus and the i-th electron, Z_a is the charge of the a-th nucleus, and M_a is the mass of the a-th nucleus, M_e is the mass of the electron. However, there is no general analytical solution to the Schrödinger equation for three or more bodies. We can use the Born-Oppenheimer approximation, where the nuclei are

doi:doi:10.6342/NTU202404801

relatively fixed, to rewrite the equation

$$\hat{H}\psi(\{\vec{r}_i\}) = [\sum_{i=1}^{N} \frac{-\hbar^2}{2M_e}\nabla_i^2 + \sum_{i=1}^{N-1}\sum_{j=i+1}^{N} \frac{e^2}{r_{ij}} + V'(\{r_i\})]\psi(\{\vec{r}_i\}) \tag{2.3}$$

, but only the electric part of the equation is still difficult to solve. In 1965, Walter Kohn and Lu Jeu Sham developed a theorem that simplifies the many-particle equation to a collection of one-particle equations. [9, 10] The first Kohn-Sham theorem states that the ground state energy of the Schrödinger equation is a unique functional of the electron density, that is

$$E_0 = E[\rho_0(\vec{r})] \tag{2.4}$$

$$\rho(\vec{r}) = \sum_{i=1}^{N} |\psi(\{\vec{r}_i\})|^2 \tag{2.5}$$

where, $\rho_0(\vec{r})$ is the ground state electron density.

The second Kohn-Sham theorem is like the variational principle, which states that

$$E[\rho(\vec{r})] \geq E_0. \tag{2.6}$$

The qual sign holds when

$$\rho(\vec{r}) = \rho_0(\vec{r}). \tag{2.7}$$

The energy functional can be written as:

$$E[\rho(\vec{r})] = T_{electron}[\rho(\vec{r})] + \frac{e^2}{2}\int \frac{\rho(\vec{r})\rho(\vec{r'})}{|\vec{r}-\vec{r'}|}d^3r d^3r' + \int V_{electron-nucleus}(\vec{r})\rho(\vec{r})d^3r$$
$$+ E_{nucleus} + E_{XC}[\rho(\vec{r})] \tag{2.8}$$

doi:doi:10.6342/NTU202404801

where $T_{electron}$ is the kinetic energy of the electron and $V_{electron-nucleus}$ is the Coulomb potential between the electron and the nucleus. The Kohn-Sham equations are as follows

$$[T_{electron} + V_H(\vec{r}) + V_{electron-nucleus}(\vec{r}) + V_{XC}(\vec{r})]\psi_i(\vec{r}) = \epsilon_i\psi_i(\vec{r}) \tag{2.9}$$

$$V_H(\vec{r}) = e^2 \int \frac{\rho(\vec{r'})}{|\vec{r} - \vec{r'}|} d^3r' \qquad \text{(Hartree potential)} \tag{2.10}$$

$$V_{XC}(\vec{r}) = \frac{\delta E_{XC}(\vec{r})}{\delta \rho(\vec{r})} \tag{2.11}$$

2.2 Exchange-Correlation Functional

The kinetic energies of the electrons, the electron-electron Coulomb potential, and the electron-nuclear Coulomb potential are well defined in the Kohn-Sham equations. The exchange-correlation energy, E_{XC}, is the only term that is difficult to understand because it includes all the remaining electronic energy components except the non-interacting kinetic and Coulomb potential terms. Although the precise form of the E_{XC}, remains unknown, accurate approximations of E_{XC} can provide reliable total energy values and other physical properties.

The simplest way to approximate the exchange correlation energy is to assume that the local electron density behaves like a uniform electron gas. Then, we have

$$E_{XC}^{LDA} = \int \epsilon_{XC}(\rho(\vec{r}))\rho(\vec{r})d^3\vec{r} \tag{2.12}$$

where the ϵ_{XC} is the exchange-correlation energy density, which is only a function of the electronic density. This is known as the local density approximation (LDA). In practical applications, LDA agrees well with many experimental results.

doi:doi:10.6342/NTU202404801

Another widely used approximation is the general gradient approximation (GGA), which considers the exchange-correlation energy density as a function of both the electronic density and its gradient. The E_{XC} can be written as

$$E_{XC}^{GGA} = \int \epsilon_{XC}(\rho(\vec{r}), \bigtriangledown\rho(\vec{r}))\rho(\vec{r})d^3\vec{r} \tag{2.13}$$

The GGA is usually better than the LAD for the transition metal with higher angular momentum electrons.

2.3 The Self-Consistent Cycle

The Kohn-Sham equations were solved using an iterative method. The self-consistent cycle in VASP is illustrated in Figure 2.1. First, the trial charge density and trial wavevector were generated. The Hamiltonian was then obtained from the previous input. Iterative refinement was then applied to the Kohn-Sham equations to solve for the new wavevectors. With the updated wavevectors, the total energy was calculated. Following this, the initial charge density was mixed with the charge density generated by the new wavevectors to calculate the new charge density. The final step in the electronic self-consistent cycle is to compare the energy of the current iteration with that of the previous loop. If the difference exceeds the required accuracy, a new loop is initiated; otherwise, the loop is closed, and the forces are calculated to update the positions of the ions.

doi:doi:10.6342/NTU202404801

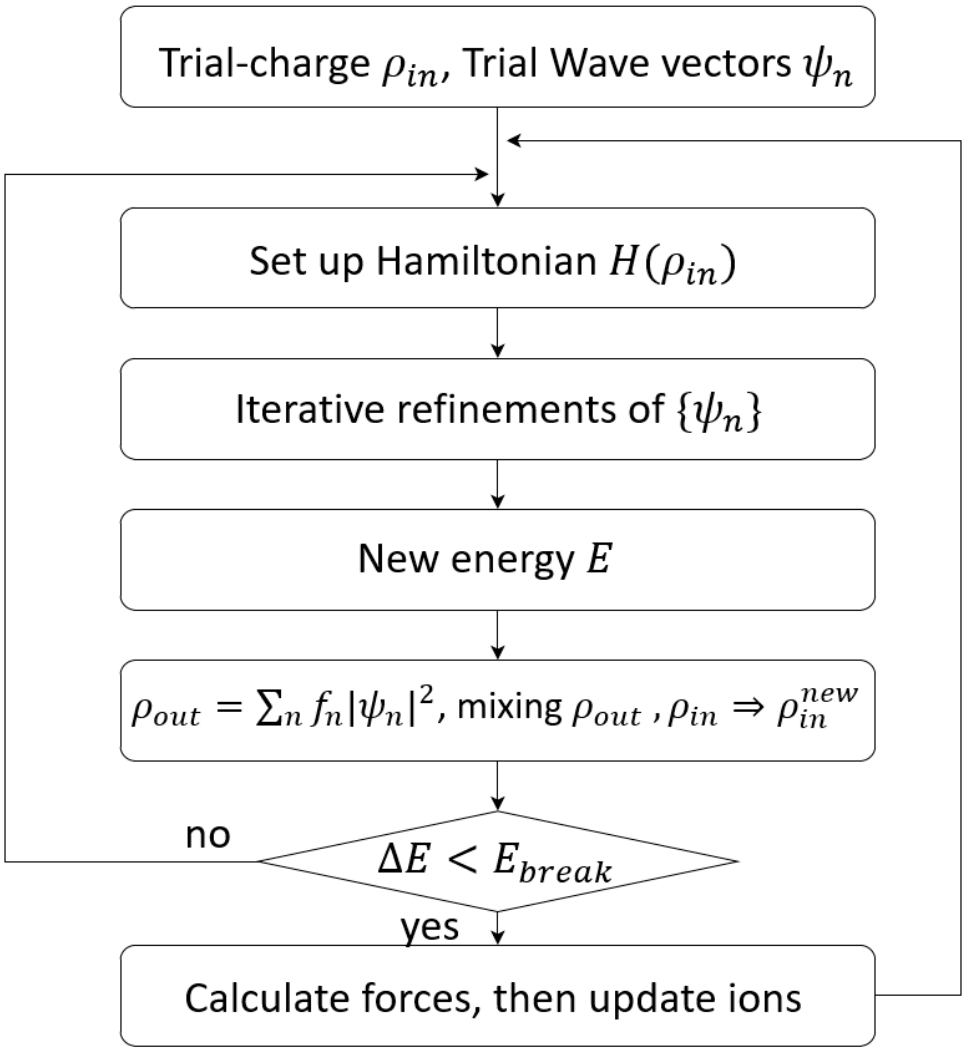

Figure 2.1: The flowchart of the ground state calculation.

doi:doi:10.6342/NTU202404801

doi:doi:10.6342/NTU202404801

Chapter 3 Driving Noncollinear Interlayer Exchange Coupling Intrinsically in Magnetic Trilayers

3.1 Introduction

Giant magnetoresistance (GMR) systems, consisting of spacer layers sandwiched between ferromagnetic layers, are widely used to fabricate a variety of spintronic devices, including spin-torque oscillators, [11, 12] magnetic random access memories,[13–15] magnetic sensors [16, 17], amd racetrack memories. [18–20] Most of these devices consist of two or more magnetic layers separated by spacer layers, and interlayer exchange coupling plays an important role in the development of spintronic devices due to its fundamental properties. [21–26]

Recent experiments on interlayer exchange couplings in metallic multilayer structures have shown that the bilinear coupling strength (J_1) and the biquadratic coupling strength (J_2) have been accurately measured in the Co/IrFe/Co structure. [27, 28] Furthermore, the noncollinear coupling has been observed in the Co/RuFe/Co structure. Since J_1

doi:doi:10.6342/NTU202404801

and J_2 vary with the thickness of the nonmagnetic intermediate layer, not only antiferromagnetic and ferromagnetic configurations of spin configurations between ferromagnetic layers can be controlled, but also non-collinear configurations can be achieved. [27] The potential for non-trivial spin alignment through noncollinear coupling holds great promise for increasing the speed and efficiency of spintronic devices. [27, 28]

Although noncollinear alignment has been observed in GMR systems, including Co/Cu/Co [29] and Fe/Cu/Fe, [30, 31] for more than 30 years. Additionally, it has been found that interface defects and film quality have hampered experimental studies of interlayer exchange coupling. [32–34] In this study, we show that unique noncollinear magnetic orientations can exist in ultrathin magnetic trilayers, consistent with recent experimental observations. J_1 was found to oscillate with spacer thickness, which could be explained by the Ruderman-Kittel-Kasuya-Yosida (RKKY) theory or the quantum well states model. However, the mechanism causing the non-collinear coupling remains poorly understood. The RKKY model is based on a model describing indirect exchange coupling of magnetic impurities within metals, [35–37] while the quantum well model suggests that spin-dependent confinement of electronic states within the spacer layer is responsible for the effective magnetic coupling between magnetic impurities. layer. [23, 38–40]

We propose that the noncollinear couplings term due to IEC, J_1 and J_2, are demonstrated employing first-principles techniques to a Fe/Ag/Fe trilayer metallic structure. By varying J_1 and J_2 with the thickness of the metallic layer, we provide a theoretical explanation consistent with recent experimental results. We also show the relationship between the ICE and the thickness of the spacer layer. We then studied quantum well states (QWS) in noncollinear systems and found that the spin of the Ag quantum well must rotate in a clockwise or counterclockwise direction perpendicular to the Fe/Ag interface. This ob-

doi:doi:10.6342/NTU202404801

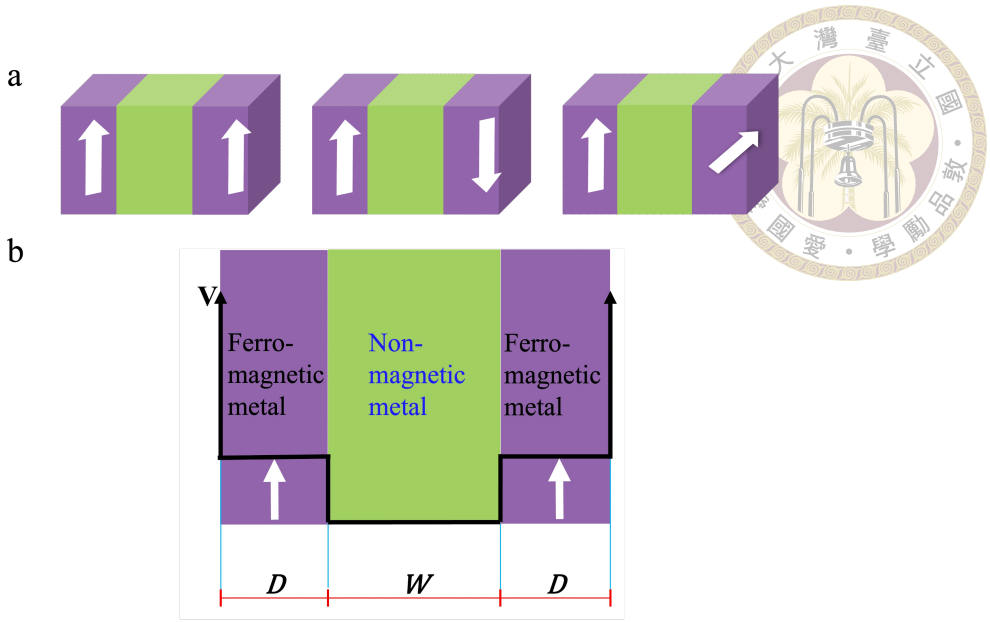

Figure 3.1: **a, Schematic illustration of the magnetic arrangement between ferromagnetic layers.** Parallel, antiparallel and perpendicular arrangements between the side ferromagnetic layers. **b, Schematic diagram of a three-layer quantum well.**

servation shows that the magnetic structure is not collinear and allows spatial rotation of carrier spins in the system, which creates important applications in the development of spintronics.

3.2 Quantum-well model

To study the GMR system in the quantum well model, we studied a three-layer metal system consisting of a nonmagnetic silver interlayer of width W and an iron side layer of width D, as shown in Figure 3.1. Magnetic coupling is associated with energy changes in different magnetic configurations corresponding to parallel, antiparallel and perpendicular arrangements of the lateral layer. The total energy per unit area of the GMR system is written as: [41]

$$E = \frac{E_F {k_F}^2}{4\pi^2} \sum_{\sigma=\uparrow,\downarrow} \sum_{n=1}^{\infty} \int d^2k_{\parallel} \frac{\frac{E(\sigma,n)}{E_F} + \frac{k_{\parallel}^2}{k_F^2} - 1}{\exp[(\frac{E(\sigma,n)}{E_F} + \frac{k_{\parallel}^2}{k_F^2} - 1)\frac{E_F}{k_B T}] + 1}, \tag{3.1}$$

doi:doi:10.6342/NTU202404801

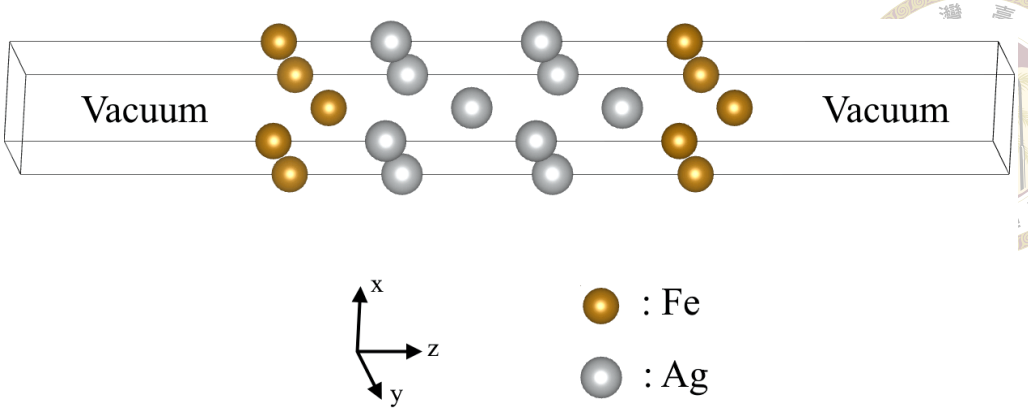

Figure 3.2: Unit cell of the $Fe_2/Ag_4/Fe_2$ trilayer.

where σ is the spin of the electron (up or down), $E(\sigma, n)$ is the energy of the n-th band, , $k_{\|}$ is the transverse wave vector, and T is the temperature.

From a phenomenological point of view, the total energy of the system per unit area is given by

$$E = -J_1(\vec{m}_1 \cdot \vec{m}_2) - J_2(\vec{m}_1 \cdot \vec{m}_2)^2, \tag{3.2}$$

where J_1 and J_2 are the IECs, and $\vec{m}_i$ is normalized magnetic moment of the i-th ferromagnetic layer. Using Eq. 3.2 to analyse the energy of the system over the three magnetic configurations, the bilinear and biquadratic IECs are as follows

$$\begin{aligned} J_1 &= -\frac{E_{AP} - E_{PA}}{2} \\ J_2 &= -\frac{E_{PA} + E_{AP}}{2} + E_N, \end{aligned} \tag{3.3}$$

In this context, E_{AP}, E_{PA}, and E_N correspond to the energies per unit area of the antiparallel, parallel, and perpendicular configurations, respectively.

doi:doi:10.6342/NTU202404801

3.3 Unit Cell and Calculation Parameters

The lattice structure of bulk Fe is body-centred cubic, whereas that of Ag is face-centred cubic. Ag(001) acts as a spacer between Fe(001) layers rotated at an angle of 45 degrees in the xy plane. The trilayers were separated by a vacuum of at least 18Å. The $Fe_2/Ag_4/Fe_2$ trilayer was visualised using VESTA (see Figure 3.2). [42] The layered structure of $Fe_2/Ag_W/Fe_2$ consists of a BCC-like unit cell consisting of two ferromagnetic monolayers (ML) on both sides and a nonmagnetic Ag layer in the middle. The silver layer thickened from 2 ML to 12 ML. The vacuum required to separate $Fe_2/Ag_W/Fe_2$ is at least 18Å. The in-plane lattice constant is 2.89 Å, and which was optimized with Ag-Bulk. The DFT calculations were performed by the Vienna Ab initio Simulation Package (VASP) [2, 43, 44] using the projector augmented wave (PAW) pseudopotentials [44] and the Perdew-Burke-Ernzerhof (PBE) generalized gradient approximation (GGA). The energy convergence criterion is defined as less than 10^{-3} meV. A gamma-centered $76\times76\times1$ K-point grid in the Brillouin zone was chosen. The energy limit for the plane wave basis is set to 350 eV. Structurally optimized unit cells were calculated using a force convergence criterion of 10^{-1} meV/Å. Nonlinear collinear calculations for three configurations (parallel, antiparallel and perpendicular orientation, see Figure 3.1) are performed without spin-orbital coupling.

3.4 Convergence Tests

To check the convergence of the bilinear interlayer exchange coupling (J_1), the collinear calculations of the $Fe_2/Ag_3/Fe_2$ structure were performed. The energy convergence crite-

doi:doi:10.6342/NTU202404801

Table 3.1: Convergence of ENCUT

ENCUT	E_{PA} (eV/unit cell)	E_{AP} (eV/unit cell)	J_1 (meV/unit cell)
270	-37.681299	-37.694752	-13.453
290	-37.710521	-37.724006	-13.485
310	-37.710612	-37.724114	-13.502
330	-37.694477	-37.707983	-13.506
350	-37.677157	-37.690658	-13.501
370	-37.664721	-37.678190	-13.469
400	-37.656335	-37.669804	-13.469
430	-37.653789	-37.667235	-13.446
460	-37.655112	-37.668553	-13.441

Table 3.2: Convergence of NGX(NGY)

NGX(NGY)	E_{PA} (eV/unit cell)	E_{AP} (eV/unit cell)	J_1 (meV/unit cell)
18	-37.677157	-37.690658	-13.501
20	-37.677216	-37.690707	-13.491
22	-37.677221	-37.690714	-13.493
24	-37.677241	-37.690737	-13.496
26	-37.677255	-37.690751	-13.496

Table 3.3: Convergence of Kpoints

K	E_{PA} (eV/unit cell)	E_{AP} (eV/unit cell)	J_1 (meV/unit cell)
40	-37.653417	-37.667001	-13.584
43	-37.653548	-37.667394	-13.846
46	-37.653506	-37.667407	-13.901
49	-37.653703	-37.667215	-13.512
52	-37.653886	-37.667337	-13.451
55	-37.653556	-37.667301	-13.745
58	-37.653835	-37.667310	-13.475
61	-37.653653	-37.667153	-13.500
64	-37.653911	-37.667387	-13.476

rion is set below 10^{-4} meV.

The parameter ENCUT, the cutoff energy for the plane wave-basis set, is checked for convergence with k-points=$76 \times 76 \times 1$. NGX (NGY), is the number of grid points in the fast Fourier transform (FFT) grid along the first (second) lattice vector, is checked with ENCUT=350 eV, also the NGZ is increased to the same ratio. The k-points ($K \times K \times 1$) are checked with NCUT=350 eV. The data of the three parameters mentioned above are shown in Table 3.1-3.3.

doi:doi:10.6342/NTU202404801

a

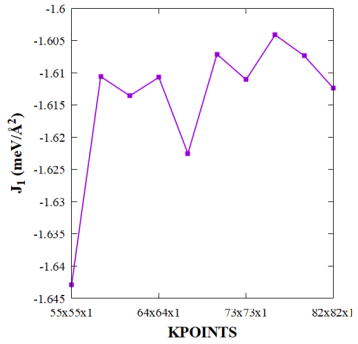

b

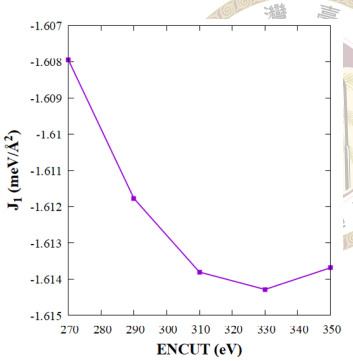

Figure 3.3: a. The J_1 versus the KPOINTS. b. The J_1 versus the ENCUT.

The J_1 calculated by different k-points and ENCUT were plotted in Figs. 3.3a and 3.3b, respectively. The J_1 varied with less than 0.01 meV/Å^2 for ENCUT greater than 270 eV and the k-points greater than $70 \times 70 \times 1$.

3.5 Results and Disscussion

Table 3.4: The energies of the different magnetic configurations for the Ag layers from 2 to 12.

W	E_{PA} (eV/unit cell)	E_N (eV/unit cell)	E_{AP} (eV/unit cell)
2	-34.956148	-34.953129	-34.955157
3	-37.655260	-37.663186	-37.668944
4	-40.379019	-40.379276	-40.378976
5	-43.123095	-43.121003	-43.119810
6	-45.840901	-45.839443	-45.838395
7	-48.561124	-48.560138	-48.558194
8	-51.275258	-51.275381	-51.276117
9	-53.993685	-53.994611	-53.995850
10	-56.759430	-56.760948	-56.761828
11	-59.487045	-59.486770	-59.486789
12	-62.213760	-62.212677	-62.211832

We optimised the $Fe_2/Ag_W/Fe_2$ trilayer structure with the antiparallel alignment of the Fe side layers with collinear spin-polarized calculations. The noncollinear calculation was then performed with the optimised structures. The energies of the different magnetic configurations, J_1, J_2, and $2|J_2|$-$|J_1|$, this determinant will be explained in the following, are are listed in Table 3.4 and Table 3.5.

doi:doi:10.6342/NTU202404801

Table 3.5: J_1, J_2, and $2|J_2|$-$|J_1|$ for the Ag layers from 2 to 12.

W	J_1 (meV/Å^2)	J_2 (meV/Å^2)	$2|J_2|$-$|J_1|$ (meV/Å^2)
2	0.118	0.302	0.485
3	-1.636	-0.130	-1.376
4	0.005	-0.033	0.061
5	0.393	0.054	-0.285
6	0.300	0.025	-0.251
7	0.350	-0.057	-0.236
8	-0.103	0.037	-0.029
9	-0.259	0.019	-0.221
10	-0.287	-0.038	-0.210
11	0.031	0.018	0.005
12	0.230	0.014	-0.202

The strengths of J_1 and J_2 in the $Fe_2Ag_WFe_2$ trilayer with different spacer widths were shown in Figure 3.4. Figure 3.4a was derived from first-principal calculations, and Figure 3.4b was derive from analytical calculations performed by the collaborator (H.-C Wang). [45] We found that the noncollinear DFT calculation shows that the noncollinear coupling dominates the ground state only in the $Fe_2Ag_4Fe_2$ structure, i.e. with the specific thickness of the nonmagnetic metal layer. The top part of Figure 3.4a shows ICEs as a function of Ag thickness, derived from Equation 3.3 by cubic spline interpolation. Note that the sign of J_1 directly represents whether parallel or antiparallel magnetic configurations are preferred. As the width of the silver layer increases, the fluctuations of J_1 and J_2 became smaller. The oscillation period of J_1 was almost twice than that of J_2, and the amplitude of J_1 was approximately seven greater than that of J_2. With increasing thickness, the amplitude of both J_1 and J_2 decreases. The results of first-principles calculations and analytical calculations are in agreement.

The extreme value of equation 3.2 occurs when $\vec{m}_1 \cdot \vec{m}_2 = cos(\theta) = -\frac{J_1}{2J_2}$, or $sin(\theta) = 0$, where the θ is the angle between the magnetic moments of the two iron layers. If the system is not in trivial magnetic alignment, then we have the discriminant: $2|J_2| - |J_1| > 0$ and $J_2 < 0$. In the DFT calculation, the discriminant holds for 4 and 11

doi:doi:10.6342/NTU202404801

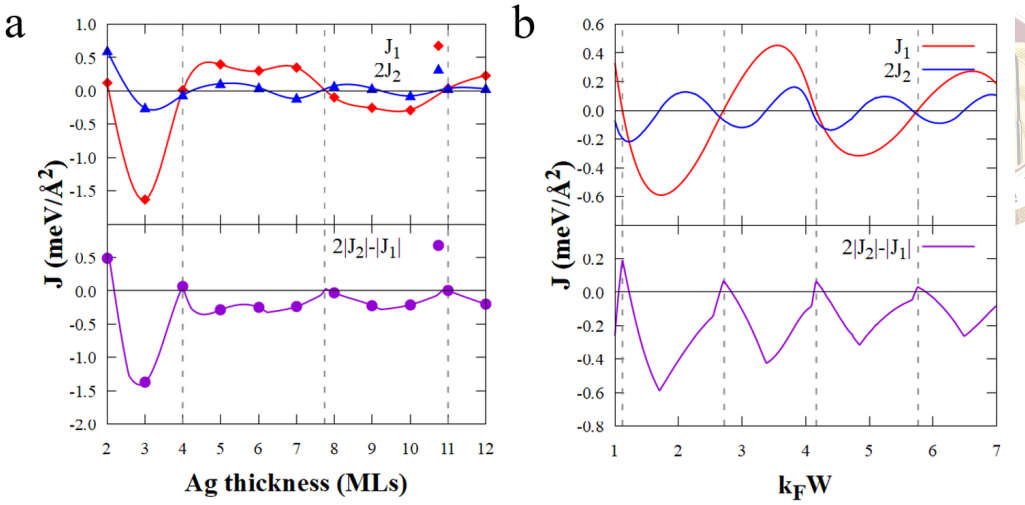

Figure 3.4: Interlayer exchange coupling between iron layers depends on the width of the intermediate silver layer. **a**, The figure above shows the bilinear and biquadratic coupling strengths J_1 (red) and J_2 (blue) calculated according to the first-rinciple. Straight lines connecting points are interpolated using cubic splines. At the bottom is the discriminator $2|J_2| - |J_1|$ (purple). **b**, Analytical calculations of J_1 (red), J_2 (blue) and $2|J_2| - |J_1|$ (purple). Where k_F is the Fermi wavevector in the silver layer and W is the width of the silver spacer layer.

MLs (see the bottom of Figure 3.4a). In fact, the energy of the three magnetic alignment in $Fe_2Ag_{11}Fe_2$ is almost degenerate, and the energy difference is smaller than the numerical error. From the result and the discriminant, when the value of J_1 is small, the noncollinear coupling is more likely to occur.

The band structure is essentially the same for both collinear and noncollinear calculations in parallel and antiparallel magnetic alignments. [39] More interesting for us is the electron in the transport direction. Thus, the band structures projected onto the p_z and d_{z^2} orbitals of the Ag atoms for W from 2 to 12 and three configurations; parallel (left), perpendicular (center) and antiparallel (right); are shown in Figs. 3.5-3.15. The color of the band represents the x component of the expected magnetization (m_x). The antiparallel magnetic systems have C_2 symmetry, so the bands are at least doubly degenerate. As the angle between the magnetic moments between the iron layers decreased to 0°, the symmetry broke and the bands split. The similar bands near the Fermi-energy rise with

doi:doi:10.6342/NTU202404801

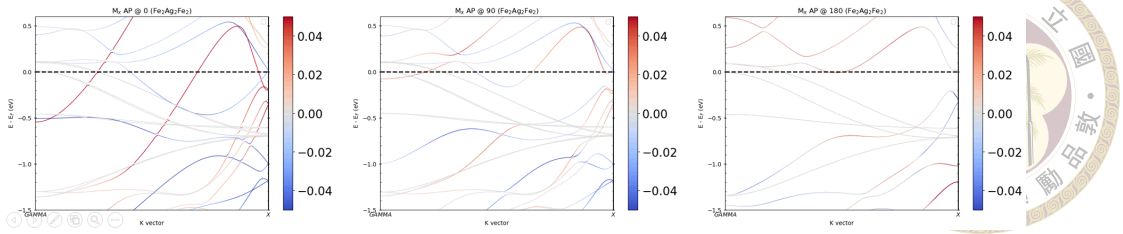

Figure 3.5: The projected band structures of the $Fe_2Ag_2Fe_2$ trilayer for the three configurations, parallel (left), perpendicular (middle) and antiparallel (right). The color of the bands represents the x-component of the projected magnetization (m_x).

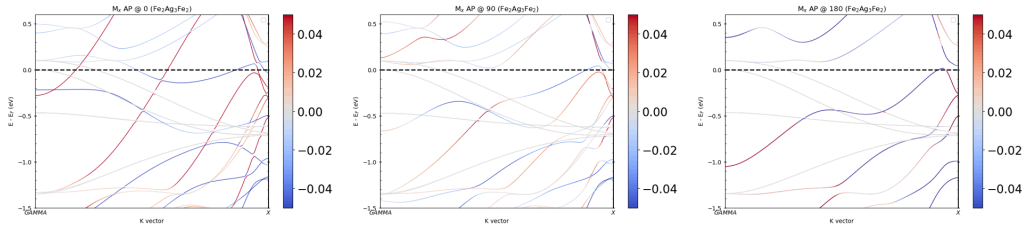

Figure 3.6: The projected band structures of the $Fe_2Ag_3Fe_2$ trilayer for the three configurations, parallel (left), perpendicular (middle) and antiparallel (right).

increasing W as the length of the transport, i.e. the thickness of the Ag spacer channel, increases.

Taking the noncollinear magnetically oriented three-layer structure $Fe_2/Ag_4/Fe_2$ as the research object, the energy band structure and spatial spin orientation of the silver quantum well are calculated to understand the characteristics of the electronic state in the non-collinear GMR system. The energy band structure of the Ag atoms p_z and d_{z^2} orbitals, relative to the transport direction, is shown in Figure 3.16a. Likewise, the color represents the x component of the projected magnetization (m_x). The electron-like quantum well state is located at the Γ points of the two energy bands marked with circles. [37, 39, 46]

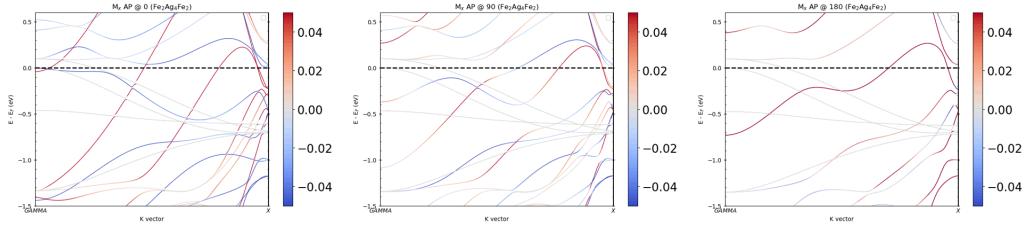

Figure 3.7: The projected band structures of the $Fe_2Ag_4Fe_2$ trilayer for the three configurations, parallel (left), perpendicular (middle) and antiparallel (right).

doi:doi:10.6342/NTU202404801

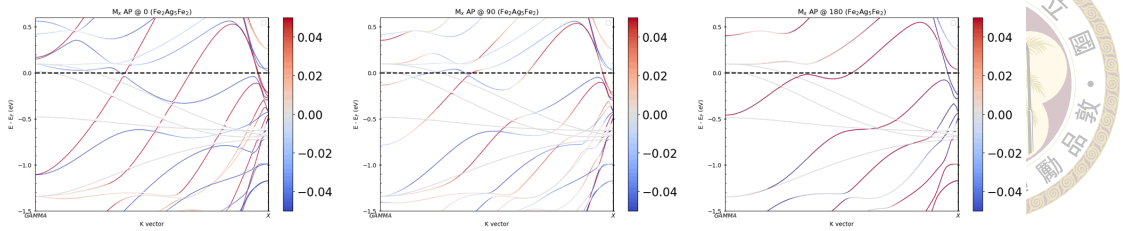

Figure 3.8: The projected band structures of the $Fe_2Ag_5Fe_2$ trilayer for the three configurations, parallel (left), perpendicular (middle) and antiparallel (right).

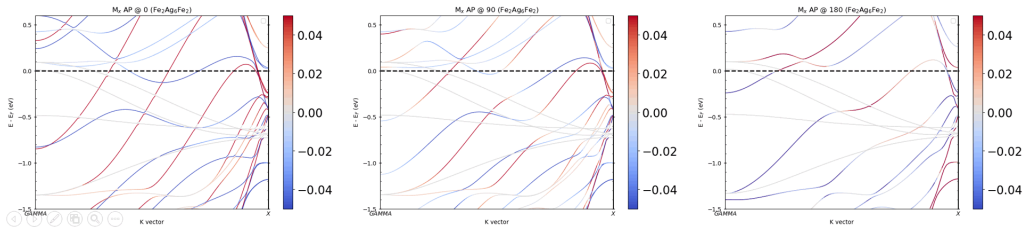

Figure 3.9: The projected band structures of the $Fe_2Ag_6Fe_2$ trilayer for the three configurations, parallel (left), perpendicular (middle) and antiparallel (right).

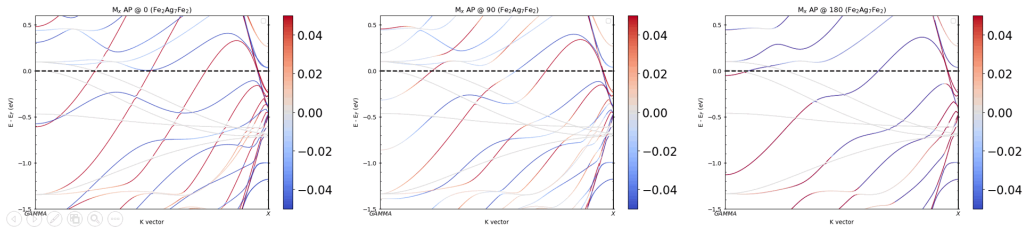

Figure 3.10: The projected band structures of the $Fe_2Ag_7Fe_2$ trilayer for the three configurations, parallel (left), perpendicular (middle) and antiparallel (right).

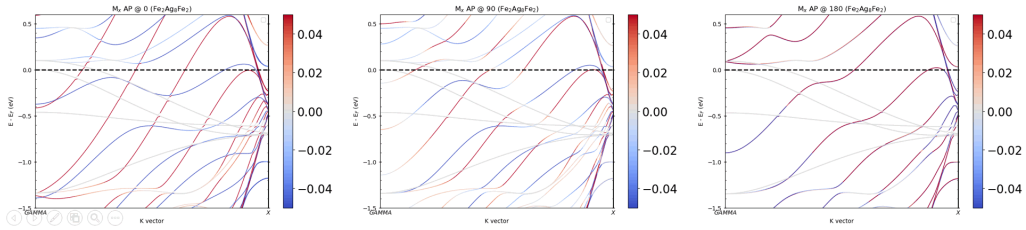

Figure 3.11: The projected band structures of the $Fe_2Ag_8Fe_2$ trilayer for the three configurations, parallel (left), perpendicular (middle) and antiparallel (right).

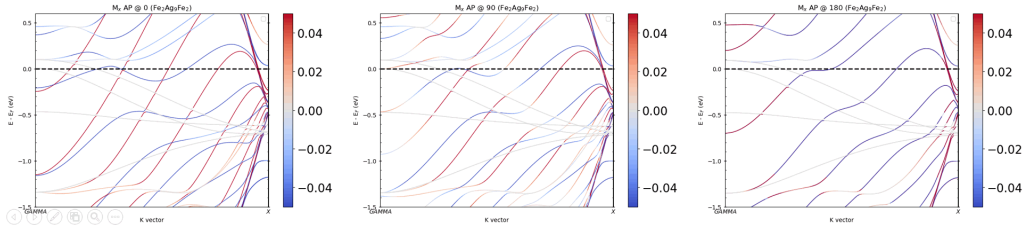

Figure 3.12: The projected band structures of the $Fe_2Ag_9Fe_2$ trilayer for the three configurations, parallel (left), perpendicular (middle) and antiparallel (right).

doi:doi:10.6342/NTU202404801

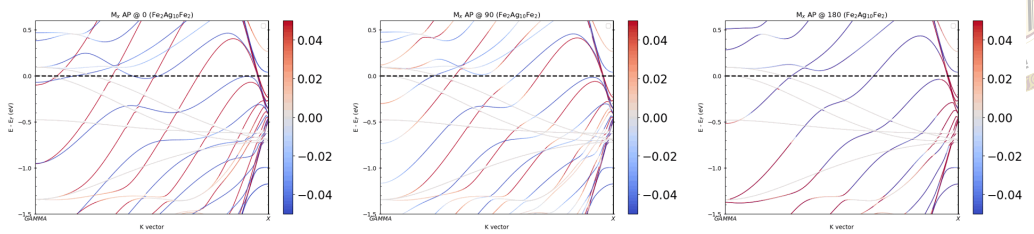

Figure 3.13: The projected band structures of the $Fe_2Ag_{10}Fe_2$ trilayer for the three configurations, parallel (left), perpendicular (middle) and antiparallel (right).

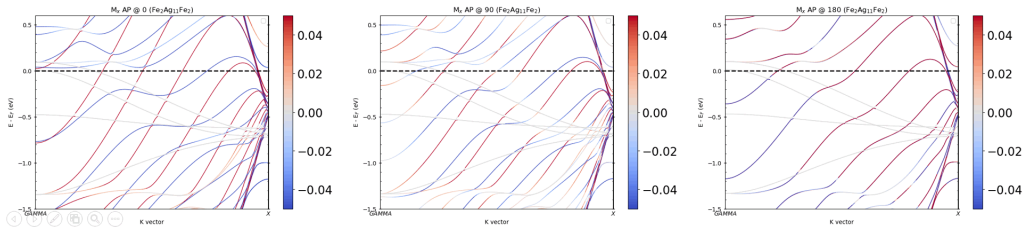

Figure 3.14: The projected band structures of the $Fe_2Ag_{11}Fe_2$ trilayer for the three configurations, parallel (left), perpendicular (middle) and antiparallel (right).

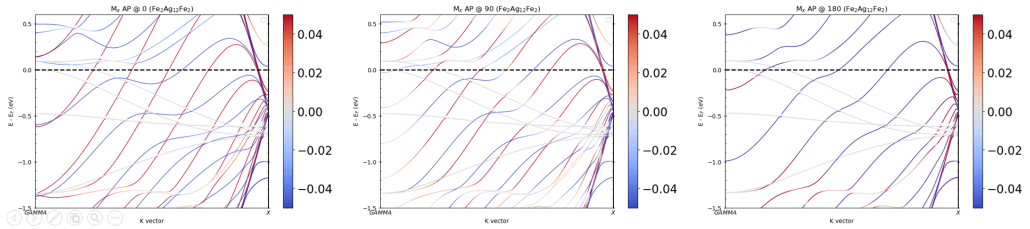

Figure 3.15: The projected band structures of the $Fe_2Ag_{12}Fe_2$ trilayer for the three configurations, parallel (left), perpendicular (middle) and antiparallel (right).

doi:doi:10.6342/NTU202404801

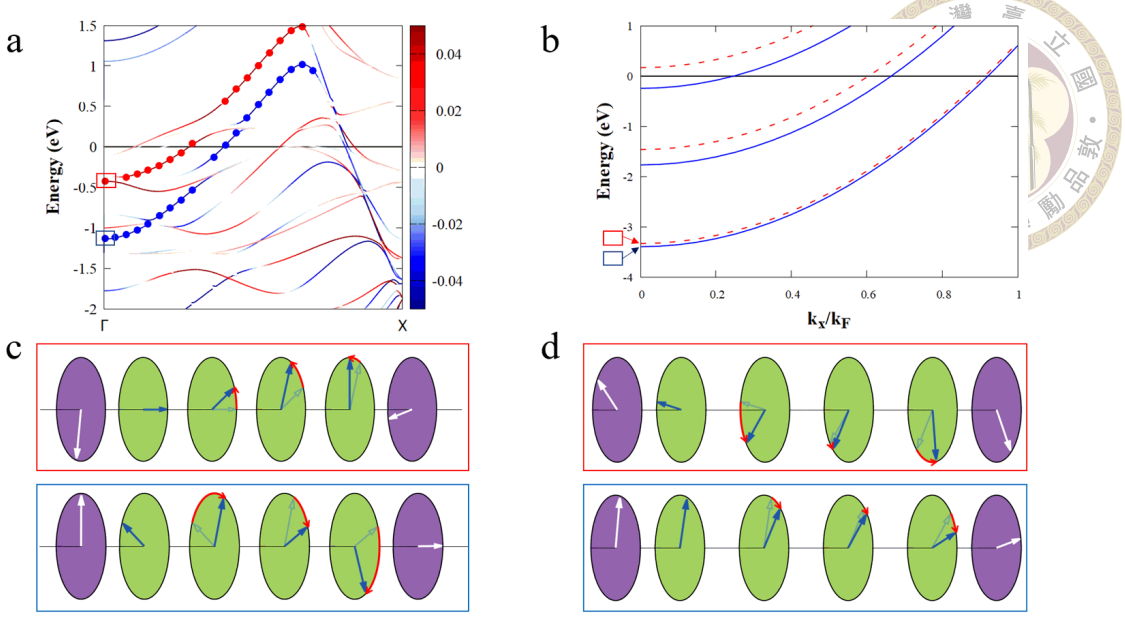

Figure 3.16: **Perpendicular magnetic alignment system band structure and spin rotation diagram.** **a**, First-principles calculations of the projected band structure of the noncollinear coupling $Fe_2/Ag_4/Fe_2$. (p_z and d_{z^2}) orbital of the silver atoms are projected. The color represents the x component of the expected magnetization (m_x). The two QWS bands are represented by the solid circles. **b**, The analytically computed band structures. The QWS band with clockwise (counterclockwise) rotation of the spin is indicated by the blue (red) line. The spin rotation plots from **c**, ab initio, and **d**, analytically derived, respectively, in accordance with the squares in Figures **a** and **b**. Arrows indicate normalized rotation in the transverse direction, and the horizontal direction indicates the direction of transmission. The coloring of the full circles indicates the different layers: green for the spacing layer(silver) and violet for the magnetic layer(iron).

As shown in Figure 3.16c, the projected magnetization of these energy bands at the Γ point rotates along the transport axis of each atom. It is worth noting that these unique bands always seem to be paired with one another. These two rotations, clockwise $90°$ and counter-clockwise $270°$, are the most striking observation to emerge from the data comparison, as they are exactly the two rotations that would result in a right $90°$ when less than a full rotation is made. This closely resembles the analytical findings on the right of the figures. (Figs. 3.16b and 3.16d). The results confirm that the spin orientation of Ag quantum well states in GMR systems with noncollinear magnetization is able to rotate in space, even in the absence of spin-orbital coupling. Figure 3.17 shows the minimum energy of the quantum well state energy band for three magnetic structures as a function

doi:doi:10.6342/NTU202404801

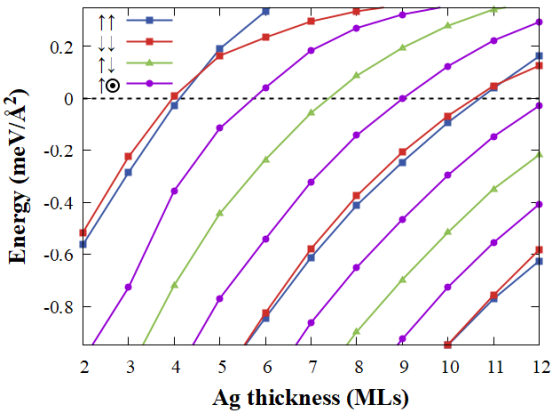

Figure 3.17: **Relationship between quantum well state energy and silver film width (D) in $Fe_2/Ag_W/Fe_2$.** For the parallel magnetized iron layers, the blue square represents the majority state of the quantum well and the red square represents the minority state of the quantum well. The green triangle corresponds to the quantum well state in the antiparallel arrangement of the iron layer.

of Ag thickness in order to relate the IECs to the quantum well resonance of the GMR system.

For the parallel magnetized iron layers, the blue square represents the majority state of the quantum well and the red square represents the minority state of the quantum well. The green triangle corresponds to the quantum well state in the antiparallel arrangement of the iron layer. Violet circles indicates the perpendicular arrangement of the iron layer. These lines connect energy points in the same quantum number. As the thickness of silver increases, the energy gap between pairs of the noncollinear alignment quantum states decreases.

When the minimum energy passes through the Fermi level (see the dotted line in Figure 3.17), the GMR system undergoes quantum resonance. For example, in a parallel magnetically aligned GMR system, if the Ag layer width is about 4 ml or 11 ml, quantum resonance occurs near the Fermi level (see blue and red squares in Figure 3.17). The quantum resonance period is about 7ML, which directly corresponds to the period of J_1 in IEC (Figure 3.4a), which is consistent with previous work. [37, 39, 46] The IEC and

doi:doi:10.6342/NTU202404801

quantum resonance have the same period in the spacer layer, and the same is true in J_2. Quantum resonance occurs in GMR magnetic systems with spacer widths of about 6 MLs and 9 MLs in perpendicular arrangement (see purple circles in Figure 3.17). The quantum resonance period is about 3 MLs, corresponding to the period of J_2 (see the top of Figure 3.4a). According to the direct correlation between Figure 3.4 and Figure 3.17, it is confirmed that by controlling the width of the GMR system, the perpendicular alignment of the GMR system can be essentially controlled.

3.6 Conclusion

In summary, we have calculated the bilinear and quadratic ICEs by using the first-principles method. This agrees with analytical calculations made by our co-worker. The results are also in agreement with previous experimental observations of the system. In addition, it has been found that the perpendicular magnetic configuration increases the degree of freedom in the choice of the magnetic structure as well as inducing the spatial spin orientation of the charge carriers. The results advance our understanding of nonlinear coupling and could aid the design of advanced spintronic devices.

doi:doi:10.6342/NTU202404801

doi:doi:10.6342/NTU202404801

Chapter 4 Electronic properties of $BiCu_2$/Cu(111)

4.1 Introduction

Spintronics is the study of the intrinsic spin, associated magnetic moment, and fundamental electron charge of electrons in solids. Spintronics uses electron spin as an additional degree of freedom for charge states, making it fundamentally different from conventional electronics. This affects the efficiency of data storage and transmission.

The conductance of $BiCu_2$ was measured by scanning tunneling spectroscopy (STS), which revealed that the conductance dI/dU is unusually large at 1.6 V.[47] We attempted to explain this phenomenon, but were unable to agree with the band structure calculated by the Korringa-Kohn-Rostoker method, which should be more accurate than the result from the Vienna Ab initio Simulation Package. Other groups have succeeded in deriving the accurate band structure and explaining the phenomeno , but we have learned a lot from this failure.

The spin topology in the $BiCu_2$ surface is unconventional compared to other surface alloys with similar structure. Most of this type of surface alloy is agree with Rashba model,

doi:doi:10.6342/NTU202404801

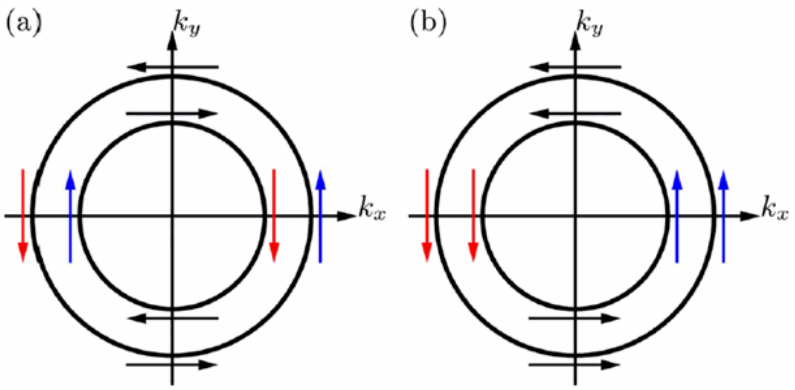

Figure 4.1: Spin-orbit separation 2DEG spin topology (schematic): (a) momentum distribution with traditional Rashba-type spin topology and (b) momentum distribution with unconventional spin topology. The ”inner” and ”outer” spin polarisations are indicated by arrows.

which explain the spin division and the antiparallel direction of the inner and outer spin, but both experiment (although it is not clear) and first principal calculation shows that the the direction of the inner and the outer spin are parallel in $BiCu_2$ (see Figure 5.1). [6]

Band structures and density of states have been calculated for bulk Cu(111) from 2 layers up to 8 layers with $BiCu_2$ on the surface. The unconventional spin topology bands we have do not agree with the result given by the Korringa-Kohn-Rostoker method, but the shape of the band structures were similar.

4.2 $BiCu_2$

The growth of Bi on the Cu(111) surface resulted in the formation of an ordered $BiCu_2$ substitution surface alloy. [48] The structure for $BiCu_2$ were accurated measured by Kaminski et al. [49] We have construct the alloy by that structure parameters and then optimzed by VASP (see Figure 4.2)

doi:doi:10.6342/NTU202404801

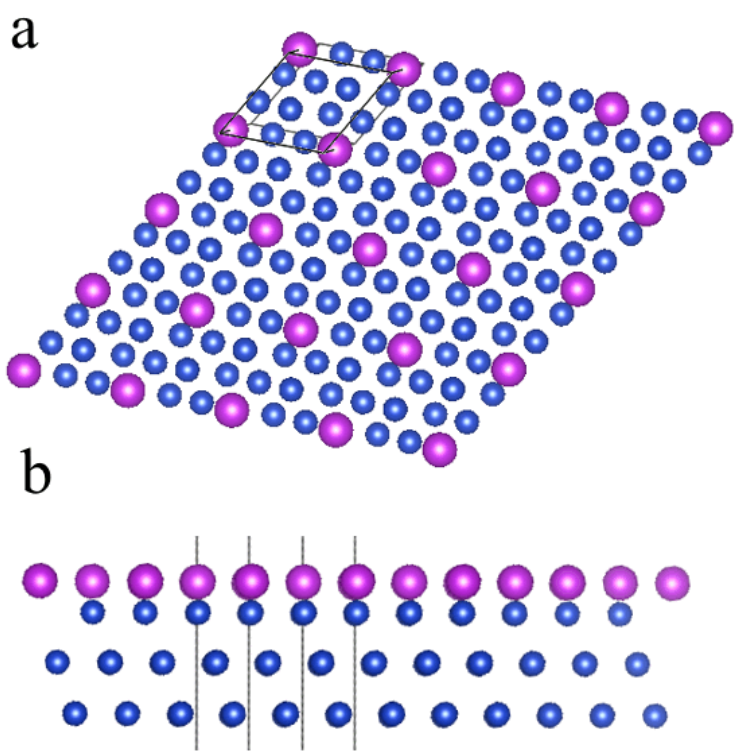

Figure 4.2: (a)Top view of $BiCu_2$ (b) Side view of $BiCu_2$

4.3 Rashiba Effect

The Hamiltonian operator with spin-orbit is

$$H = \frac{1}{2}\hat{p}^2 + V(r) + \frac{1}{2c^2}\vec{\sigma}\cdot[\bigtriangledown V(r)\times\vec{p}] \tag{4.1}$$

$$= -\frac{1}{2}\bigtriangledown^2 + i\frac{\partial_z V(x)|_{z=0}}{2c^2}(\sigma_x\partial_y - \sigma_y\partial_x) \tag{4.2}$$

doi:doi:10.6342/NTU202404801

[50], which comes from

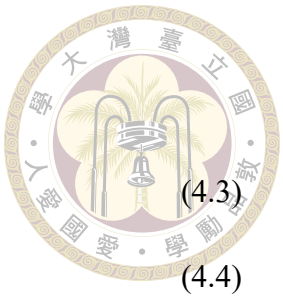

$$H_m = -\vec{\mu} \cdot \vec{B} \tag{4.3}$$

$$\vec{B} = -\frac{\vec{v} \times \vec{E}}{c^2} \tag{4.4}$$

$$\vec{v} = \frac{\vec{p}}{m} \tag{4.5}$$

$$\vec{E} = \bigtriangledown V \tag{4.6}$$

$$\vec{\mu} = -\frac{g_s \mu_B \vec{S}}{\hbar} = -\frac{g_s \mu_B \vec{\sigma}}{2} \tag{4.7}$$

This Hamiltonian is non-relativistic. We assume that the electrons in the alloy surface are a two-dimensional electron gas, i.e. V=V(z), which is independent of the x, y component. Then we can simplify and extract the Rashiba term of the Hamiltonian

$$H_R = \alpha(\vec{\sigma} \times \vec{k}) \cdot \hat{z} \tag{4.8}$$

$$= \alpha(\sigma_x k_y - \sigma_y k_x) \tag{4.9}$$

$$= \alpha \begin{pmatrix} 0 & k_y + ik_x \\ k_y - ik_x & 0 \end{pmatrix} \tag{4.10}$$

Solving this Hamiltonian we get

$$E_\pm = \frac{\hbar^2 k^2}{2m^*} \pm \alpha|\vec{k}|, \vec{k} = (k_x, k_y) \tag{4.11}$$

Assume that the eigenfunctions consist of a plane-wave spinor,

$$\psi_k(r) = (\mu_k \chi^+ + \nu_k \chi^-) e^{i(k_x x + k_y y)} \tag{4.12}$$

doi:doi:10.6342/NTU202404801

The Pauli spinors χ± are quantized with respect to the z-axis, i.e,

$$\sigma_z \chi^{\pm} = \pm \chi^{\pm} \tag{4.13}$$

$$\sigma_x \chi^{\pm} = \pm \chi^{\mp} \tag{4.14}$$

$$\sigma_y \chi^{\pm} = \pm i \chi^{\mp} \tag{4.15}$$

Substituting ψ into Schrödinger's equation, we have

$$(k_y + ik_x)\nu_k^2 = (k_y - ik_x)\mu_k^2 \tag{4.16}$$

$$\mu_{k\pm} = \frac{1}{\sqrt{2}} \tag{4.17}$$

$$\nu_{k\pm} = \mp \frac{1}{\sqrt{2}} \sqrt{\frac{k_y - ik_x}{k_y + ik_x}}, \text{ for k}\neq 0 \tag{4.18}$$

The spin polarization is complete and normal to k, so P is written as follows

$$P_{\pm}(k) = \psi_{k\pm} \sigma \psi_{k\pm} \tag{4.19}$$

$$= \pm \frac{1}{|k|} \begin{pmatrix} k_y \\ k_x \\ 0 \end{pmatrix} \tag{4.20}$$

The above equation corresponds to the spin topology of Figure 4.1(a).

4.4 Result and Discussion

The DFT calculations were carried out with the Vienna Ab initio Simulation Package (VASP). [2, 43, 44] The pseudopotentials used were the Projector Augmented Wave (PAW) pseudopotentials [44] and the Perdew-Burke-Ernzerhof (PBE) generalized gra-

doi:doi:10.6342/NTU202404801

Table 4.1: The energy of the unit cell for different vacuum thicknesses.

Thickness (Å)	15	20	25	30
E_0 (eV/unit cell)	-32.0389	-32.0379	-32.0376	-32.0373

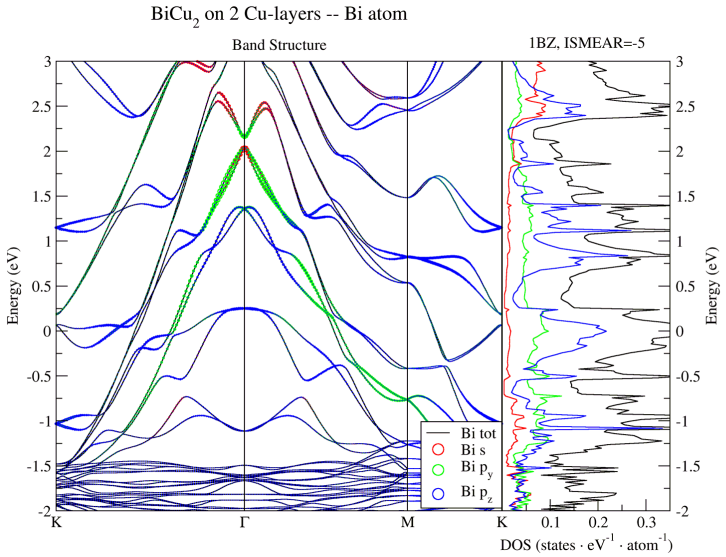

Figure 4.3: The projected band structures and density of states of $BiCu_2$ on 2 layers of Cu(111) on Bi atoms. The size of the color circle indicates the weight of density of states of the s (red), p_y (green) and p_z (blue) orbitals.

dient approximation (GGA). Less than 10^{-1} meV was used as the energy convergence criterion. The Brillouin zone was sampled using an $11 \times 11 \times 1$ k-point mesh centred on gamma. A 450 eV energy cutoff was used for the plane-wave basis. The collinear calculation with an energy convergence criterion of 1 meV without spin-orbital coupling was used to obtain the structurally optimised unit cells. For the calculations of the band structure and the density of states, the spin-orbital coupling is included and the non-collinear calculation is carried out.

We have checked the convergence of the vacuum thickness. According to Table 4.1, 15Å is thick enough for this system.

The projected band structures and density of states of $BiCu_2$ on 2, 4, 6, and 8 layers of Cu(111) on Bi atoms are shown in Figs. 4.3-4.6. The size of the color circle indicates the weight of density of states of the s (red), p_y (green) and p_z (blue) orbitals.

doi:doi:10.6342/NTU202404801

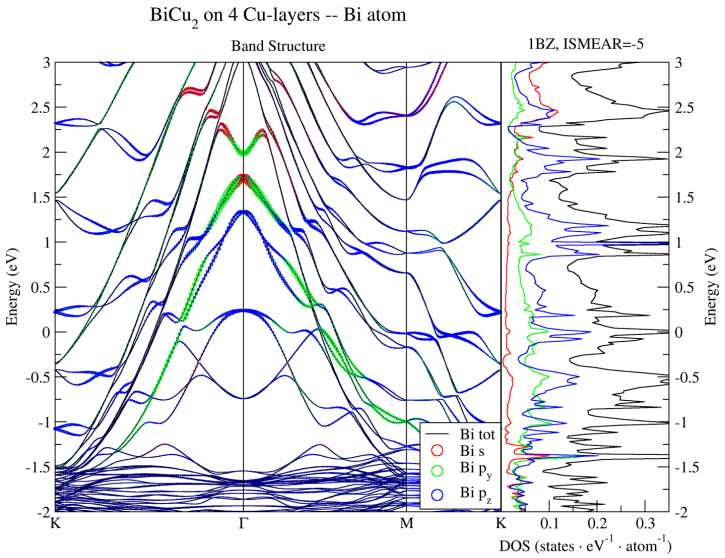

Figure 4.4: The projected band structures and density of states of $BiCu_2$ on 4 layers of Cu(111) on Bi atoms.

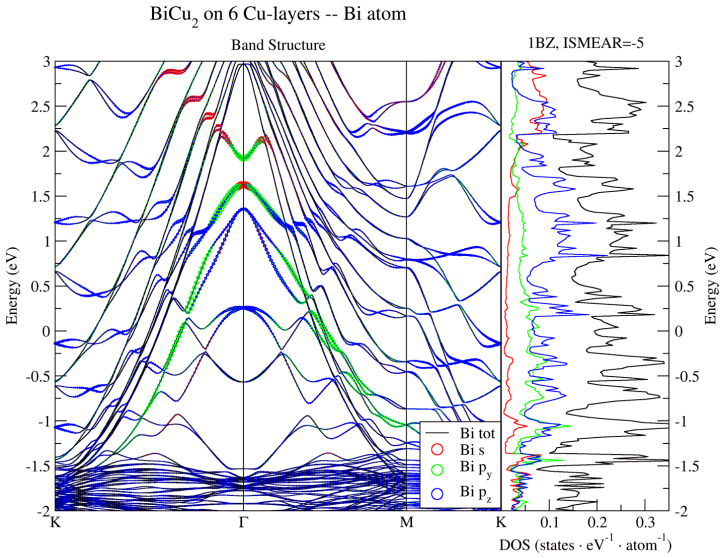

Figure 4.5: The projected band structures and density of states of $BiCu_2$ on 4 layers of Cu(111) on Bi atoms.

doi:doi:10.6342/NTU202404801

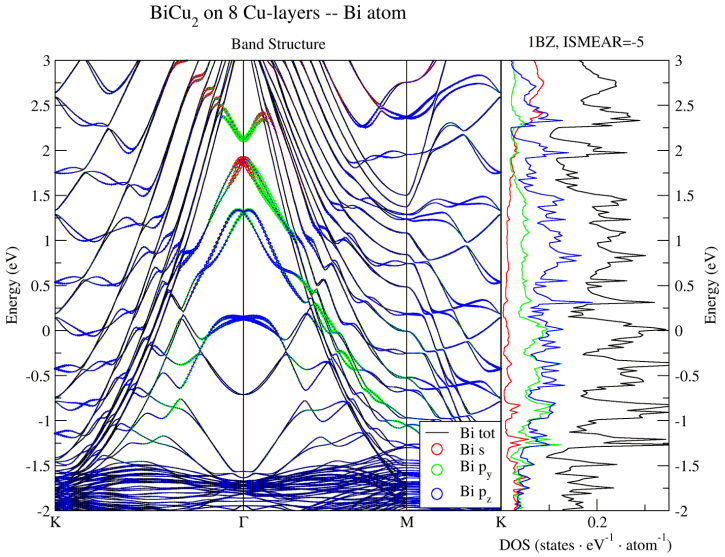

Figure 4.6: The projected band structures and density of states of $BiCu_2$ on 4 layers of Cu(111) on Bi atoms.

The spin-resolved band structures of $BiCu_2$ on 2, 4, 6, and 8 layers of Cu(111) for k_x are shown in Figs. 4.7-4.10. The color indicates the strength of y component of the magnetic moment.

The density of states does not increase significantly around 1.6 eV, but in the experiment the conductivity increases rapidly at 1.6 V. In general, there is an unconventional band around 1.7 eV. a However, in the case of 6 Cu layers, the unconventional band almost becomes a conventional band. Another group, using the LDA exchange correlation functional and 9 layers of Cu, constrained the height of the surface Bi atom and obtained a better band structure and density of states. [47]

doi:doi:10.6342/NTU202404801

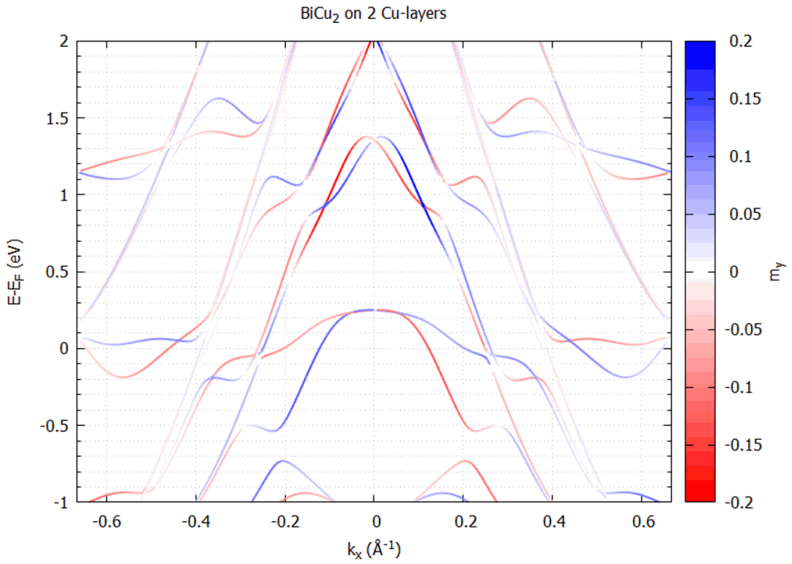

Figure 4.7: The spin-resolved band structures of $BiCu_2$ on 2 layers of Cu(111) for k_x. The color indicates the strength of y component of the magnetic moment.

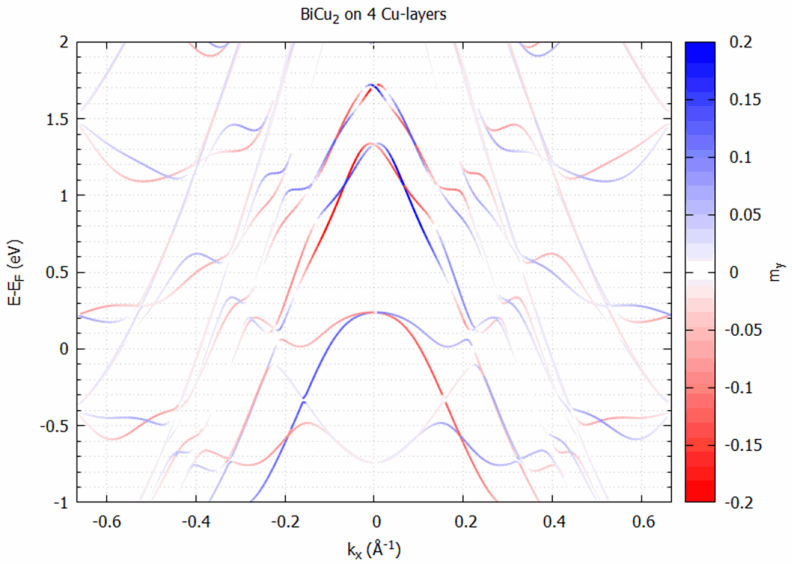

Figure 4.8: The spin-resolved band structures of $BiCu_2$ on 4 layers of Cu(111) for k_x.

doi:doi:10.6342/NTU202404801

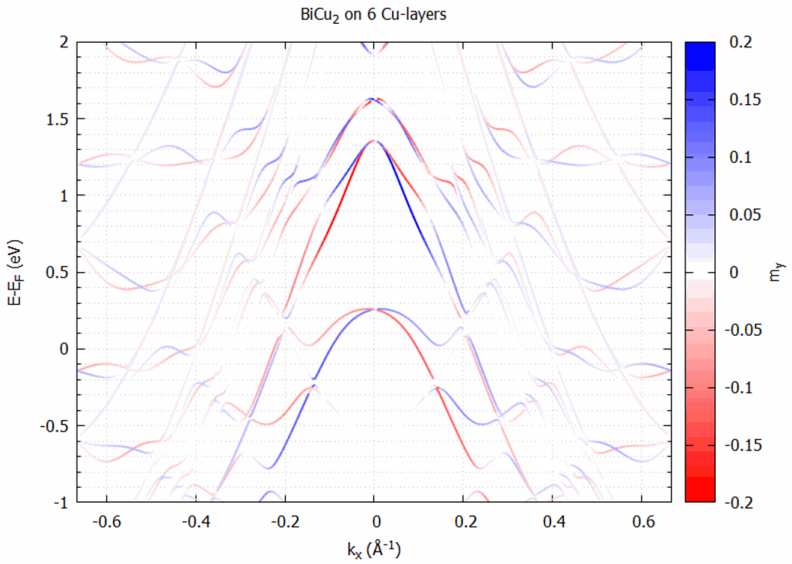

Figure 4.9: The spin-resolved band structures of $BiCu_2$ on 6 layers of Cu(111) for k_x.

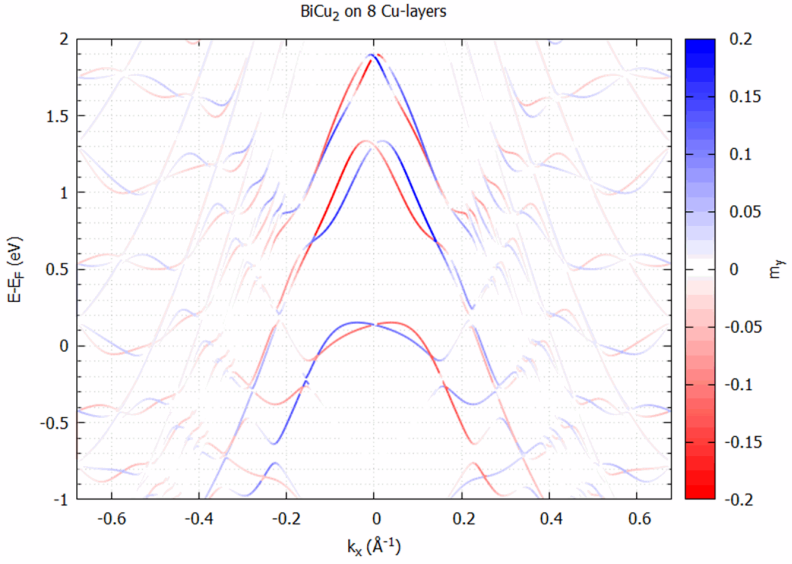

Figure 4.10: The spin-resolved band structures of $BiCu_2$ on 8 layers of Cu(111) for k_x.

doi:doi:10.6342/NTU202404801

Chapter 5 Adsorption Energies of Chiral Peptides on an Au/Co Surface

5.1 Introduction

Magnetic force microscopy is a technique for detecting the magnetic moment on a surface. It is usually the magnetic dipole-dipole interaction between the tip of the probe and the surface of the material. The distance between the tip and the surface is relatively small because the strength of the interaction is proportional to r_3. Amir Ziv et al. propose a new method using a chiral peptide to probe the spin moment of the surface. [7] The spin-exchange interaction between the chiral peptide and the surface is quite different for different spin orientations. The energy difference between different spin orientations. is about 152 meV.

We first constructed the unit cell including the tail of the peptide and the Au/Co surface. We then calculated the energy with different spin orientations, but the energy still did not agree with the experiment.

doi:doi:10.6342/NTU202404801

5.2 Chiral Induced Spin Selectivity Effect

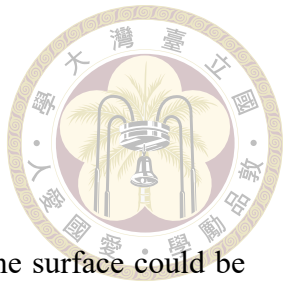

The spin-exchange interaction between the chiral peptide and the surface could be the Chiral Induced Spin Selectivity (CISS) effect. As the chiral peptide approaches the surface, the magnetic moment from the surface acting on the chiral peptide redistributes the charge in the peptide. Both the electric and magnetic fields are induced by the redistribution of charge. The induced magnetic field is different for different chirals. This causes the energy to differ between the spin orientations. The Hamiltonian of the spin-orbital interaction can be described by

$$H_{SO} = \lambda \vec{\sigma} \cdot (\vec{p} \times \vec{E}_c hiral) \tag{5.1}$$

5.3 Unit Cell of peptide on Au/Co

The chiral peptide is called alpha helix polyalanine (AHPA) in the reference. The chemical form of AHPA is HS-PEG-NH-AAAAKAAAAKAAAAKAAAAKAAAAKAAAAKAAAAK-COOH. The whole peptide is too large to calculate, so we constructed only the tail, AAAAKAAAAKAAAAK-COOH. The positional information of the L-chiral peptide, AAAAKAAAAKAAAAK-COOH, is generated by "Avogadro", and optmized by VASP. The -COOH tail has been rotated to lower the oxygen atom, giving lower energy and a better expected interaction with the surface (see Figure 5.1 and Figure 5.2).

The surface in the experiment is coated with Au to prevent oxidation of Co. The lattice mismatch of Au/Co(111) is large for the small unit cell, but the large unit cell is too expensive to calculate. The strain energy is reduced by creating a Co transition layer.

doi:doi:10.6342/NTU202404801

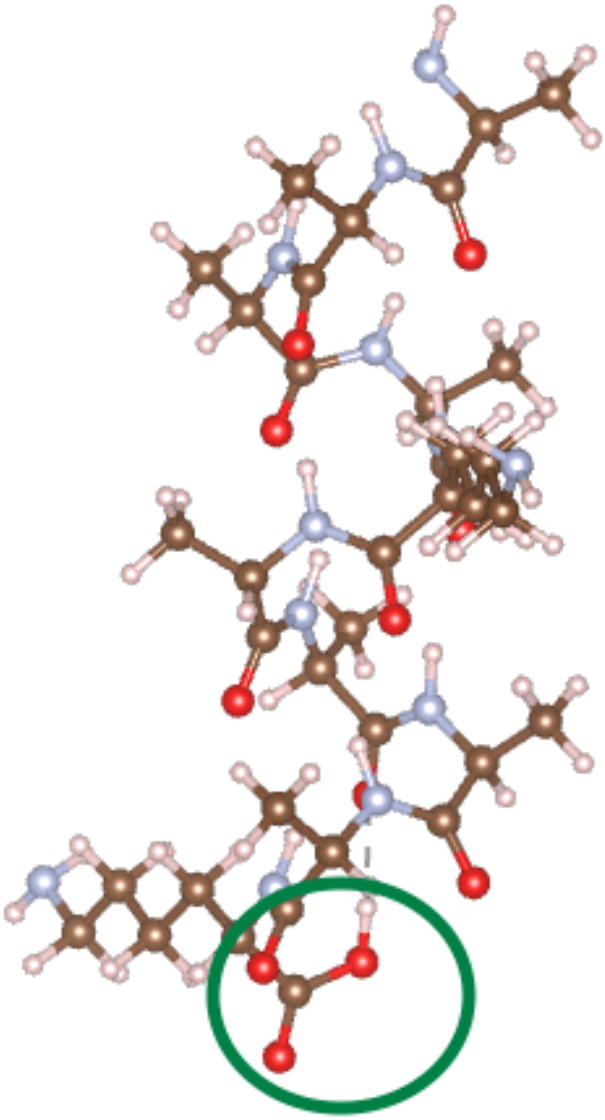

Figure 5.1: The L-AAAAKAAAAK-COOH molecule.

[51] The unit cell of the surface is constructed with one Au layer and two Co layers, and the one Co atom is removed and the Co atoms are rearranged in the first Co layer as a transition layer (see Figure 5.3).

doi:doi:10.6342/NTU202404801

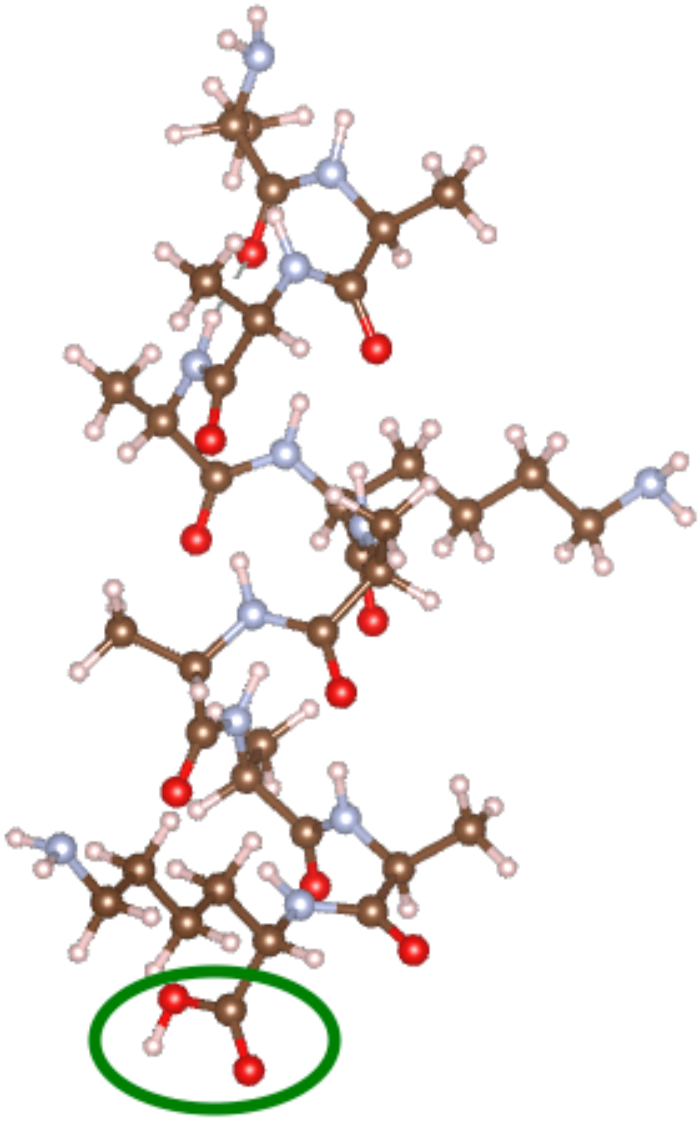

Figure 5.2: The L-AAAAKAAAAK-COOH molecule has undergone optimisation of the rotation of the -COOH tail.

5.4 Result and Discussion

The Vienna Ab initio Simulation Package (VASP) was used to perform the DFT calculations. [2, 43, 44], using PAW pseudopotentials and Perdew-Burke-Ernzerhof (PBE) GGA. [44] The criterion for the energy convergence has been set to be less than 10^{-2} meV. The Brillouin zone was sampled using a $1 \times 1 \times 1$ k-point gamma-centred mesh. The plane-wave basis energy threshold was set at 520 eV. The collinear calculation with

doi:doi:10.6342/NTU202404801

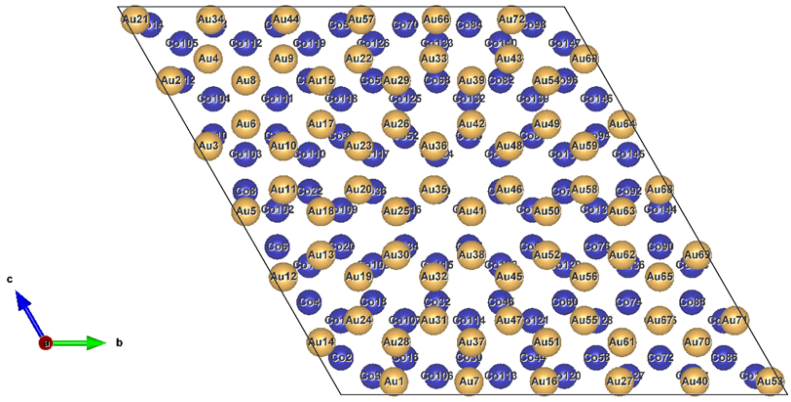

Figure 5.3: The unit cell of the peptide (L-AAAAKAAAAK-COOH) on the Au/Co surface.

Table 5.1: The total energy and magnetic moment with different spin.

Co spin orientation	Spin-up	Spin-down
Energy (eV)	-1918.762	-1918.762
Magnetic Moment (a.u.)	241.36	-241.36

the energy convergence criterion of 10^{-1} meV without spin-orbital coupling was used to obtain the structurally optimised unit cells. Note that the Co atoms are fixed.

The total energy of L-AAAAKAAAAK-COOH on Au/Co(111) with different spin is given in Table 5.1. The energies are identical, so we include the spin-orbital coupling and recalculate (see Table 5.2).

The energy difference is still very small.

The height of the peptide plays an important role in this interaction, so we optimised the system with different heights of the peptide without spin-orbital coupling. The optimiezed hight and total energy are listed in Table 5.3.

The energies difference at similar optimized hight is still very small. We also tried to increase the length of the peptide, L-AAAAKAAAAKAAAAK-COOH, (see Table 5.4).

Table 5.2: The total energy with different spin including spin-orbital coupling.

Co spin orientation	Spin-up	Spin-down
Energy (eV)	-1940.282	-1940.273

doi:doi:10.6342/NTU202404801

Table 5.3: The optimiezed hight and total energy with different spin

L-peptide	Spin-up						
Hight (Å)	3.942	3.689	3.5394	2.698	2.515	2.375	2.204
Energy (eV)	-1918.866	-1918.881	-1918.888	-1918.938	-1918.96	-1918.964	-1918.938
L-peptide	spin-dw						
Hight (Å)	3.942	3.693	3.538	2.698	2.507	2.344	2.123
Energy (eV)	-1918.867	-1918.877	-1918.889	-1918.934	-1918.954	-1918.956	-1918.908

Again, the results are not in agreement with the experiment.

Table 5.4: The total energy with different spin for L-AAAAKAAAAKAAAAK-COOH.

	Energy (eV)	Difference (eV)
Spin-up	-2286.327	
Spin-down	-2286.3251	0.0019
Spin-up with SOC	-2307.1045	
Spin-down with SOC	-2307.1055	-0.001

In order to observe the variation in electronic structure that is induced by the direction of the magnetic moment, the charge density difference for both cases is plotted.

$$\Delta\rho = \rho(\text{peptide on Au/Co}) - \rho(\text{peptide}) - \rho(\text{Au/Co}) \tag{5.2}$$

Figure 5.4 and Figure 5.5 illustrate the charge density difference of the peptide (L-AAAAKAAAAK-COOH) on the Au/Co, with the direction of the spin of Co being up and down, respectively. The isosurface has been set to $2 \times 10^{-4} e/\text{Bohr}^3$. It is evident from the figures that the difference between the two cases is very similar to each other, as are the total energies (see Table 5.1).

The calculations demonstrate that the difference in electric properties between the spin of Co being up and down is not significant. This may be attributable to the inadequacy of the unit cell or the insufficient rigour of the energy convergence criteria.

doi:doi:10.6342/NTU202404801

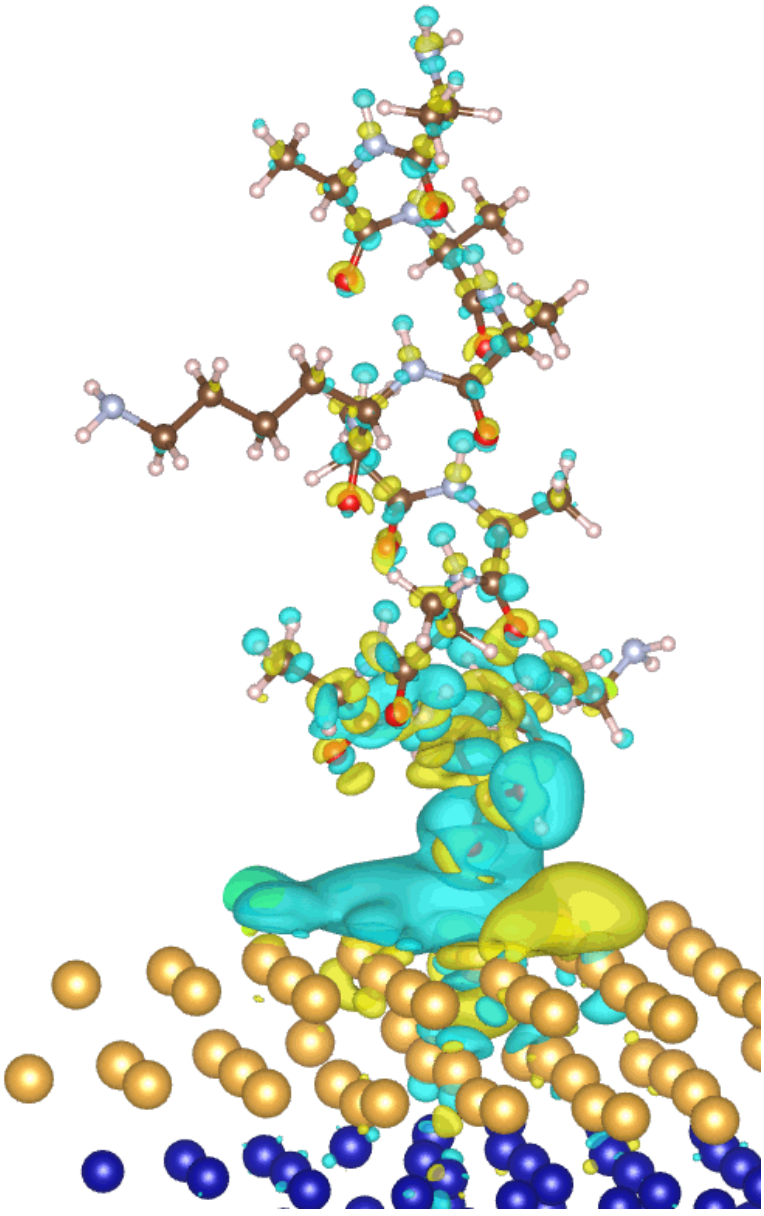

Figure 5.4: The charge density difference of the peptide (L-AAAAKAAAAK-COOH) on the Au/Co with Co spin-up.

doi:doi:10.6342/NTU202404801

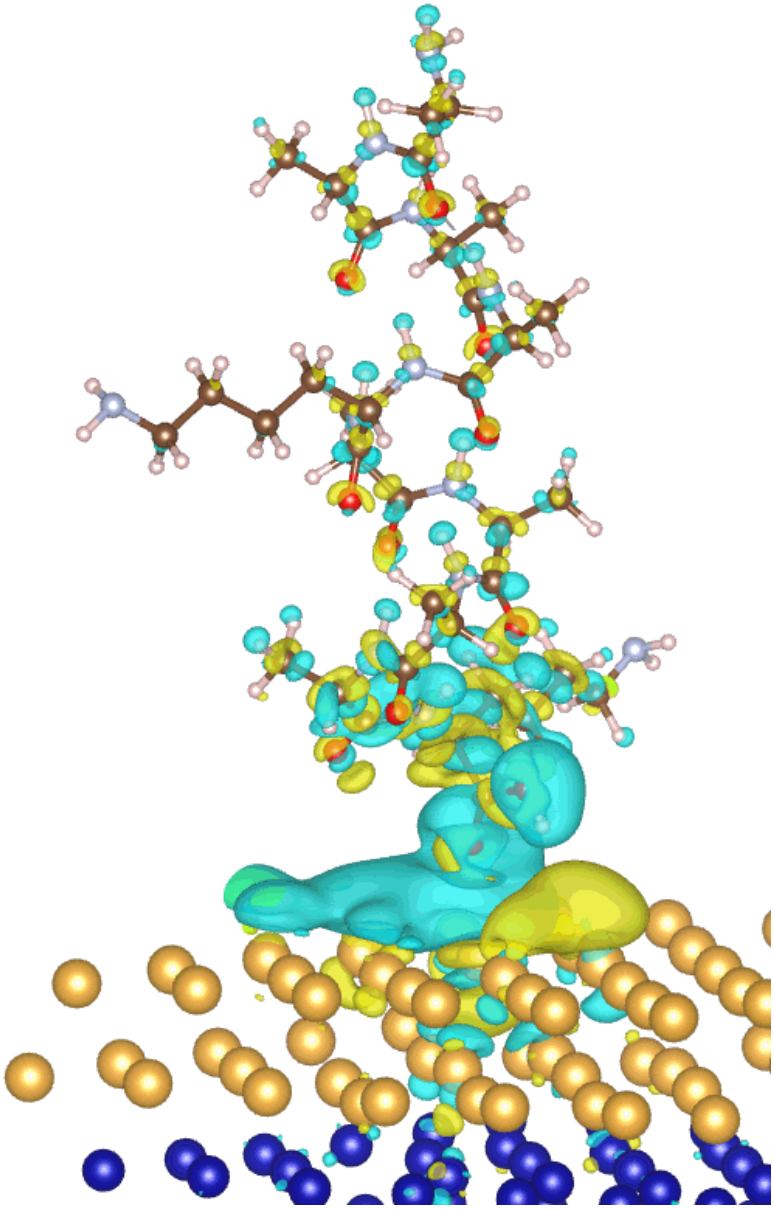

Figure 5.5: The charge density difference of the peptide (L-AAAAKAAAAK-COOH) on the Au/Co with Co spin-down.

doi:doi:10.6342/NTU202404801

Chapter 6 Summary and Conclusion

In the Fe/Ag/Fe thin film system, the magnetic configurations of the ground state may be more than parallel and anti-parallel, with a perpendicular configuration also being a possibility. In the state with a perpendicular configuration, the rotation of the magnetic moment can also be in two ways: clockwise and anti-clockwise. These physical properties are of high potential application in spintronic devices.

The LDA exchange correlation energy functional was found to be superior in predicting the band structure of the $BiCu_2$ alloy. However, GGA is typically more accurate in magnetic systems.

The following potential rationales may be postulated to explain the energy of the peptide on Au/Co: 1. The optimised distance between the peptide and the surface may have been erroneously calculated. 2. The energy convergence may have been inadequate to attain the ground state and correct shape of the peptide.

doi:doi:10.6342/NTU202404801

doi:doi:10.6342/NTU202404801

References

[1] G. Kresse and J. Hafner. Ab initio molecular dynamics for liquid metals. Phys. Rev. B, 47:558–561, Jan 1993.

[2] G. Kresse and J. Furthmüller. Efficiency of ab-initio total energy calculations for metals and semiconductors using a plane-wave basis set. Computational Materials Science, 6(1):15–50, 1996.

[3] G. Kresse and J. Furthmüller. Efficient iterative schemes for ab initio total-energy calculations using a plane-wave basis set. Phys. Rev. B, 54:11169–11186, Oct 1996.

[4] G. Kresse and D. Joubert. From ultrasoft pseudopotentials to the projector augmented-wave method. Phys. Rev. B, 59:1758–1775, Jan 1999.

[5] Hung-Chin Wang. Origin of intrinsic biquadratic magnetic exchange coupling in giant-magnetoresistance system. Master's thesis, National Cheng Kung University, 2024.

[6] H. Mirhosseini, J. Henk, A. Ernst, S. Ostanin, C.-T. Chiang, P. Yu, A. Winkelmann, and J. Kirschner. Unconventional spin topology in surface alloys with rashba-type spin splitting. Phys. Rev. B, 79:245428, Jun 2009.

[7] Amir Ziv, Abhijit Saha, Hen Alpern, Nir Sukenik, Lech Tomasz Baczewski, Shira

doi:doi:10.6342/NTU202404801

Yochelis, Meital Reches, and Yossi Paltiel. Afm-based spin-exchange microscopy using chiral molecules. Advanced Materials, 31(40):1904206, 2019.

[8] E. Schrödinger. An undulatory theory of the mechanics of atoms and molecules. Phys. Rev., 28:1049–1070, Dec 1926.

[9] W. Kohn and L. J. Sham. Self-consistent equations including exchange and correlation effects. Phys. Rev., 140:A1133–A1138, Nov 1965.

[10] What is Density Functional Theory?, chapter 1, pages 1–33. John Wiley & Sons, Ltd, 2009.

[11] Joo-Von Kim. Spin-torque oscillators. In Solid State Physics, volume 63, pages 217–294. Elsevier, 2012.

[12] Tingsu Chen, Randy K Dumas, Anders Eklund, Pranaba K Muduli, Afshin Houshang, Ahmad A Awad, Philipp Dürrenfeld, B Gunnar Malm, Ana Rusu, and Johan Åkerman. Spin-torque and spin-hall nano-oscillators. Proceedings of the IEEE, 104(10):1919–1945, 2016.

[13] Ricardo C Sousa and I Lucian Prejbeanu. Non-volatile magnetic random access memories (mram). Comptes Rendus Physique, 6(9):1013–1021, 2005.

[14] Andrew D Kent and Daniel C Worledge. A new spin on magnetic memories. Nature Nanotechnology, 10(3):187–191, 2015.

[15] Sabpreet Bhatti, Rachid Sbiaa, Atsufumi Hirohata, Hideo Ohno, Shunsuke Fukami, and SN Piramanayagam. Spintronics based random access memory: a review. Materials Today, 20(9):530–548, 2017.

doi:doi:10.6342/NTU202404801

[16] Roland Weiss, Roland Mattheis, and Günter Reiss. Advanced giant magnetoresistance technology for measurement applications. Measurement Science and Technology, 24(8):082001, 2013.

[17] Mohammed Asadullah Khan, Jian Sun, Bodong Li, Alexander Przybysz, and Jürgen Kosel. Magnetic sensors-a review and recent technologies. Engineering Research Express, 3(2):022005, 2021.

[18] Stuart SP Parkin, Masamitsu Hayashi, and Luc Thomas. Magnetic domain-wall racetrack memory. science, 320(5873):190–194, 2008.

[19] Stuart Parkin and See-Hun Yang. Memory on the racetrack. Nature Nanotechnology, 10(3):195–198, 2015.

[20] See-Hun Yang, Kwang-Su Ryu, and Stuart Parkin. Domain-wall velocities of up to 750 m s- 1 driven by exchange-coupling torque in synthetic antiferromagnets. Nature Nanotechnology, 10(3):221–226, 2015.

[21] Kang Wang, Vineetha Bheemarasetty, and Gang Xiao. Spin textures in synthetic antiferromagnets: Challenges, opportunities, and future directions. APL Materials, 11(7), 2023.

[22] See-Hun Yang and Stuart Parkin. Novel domain wall dynamics in synthetic antiferromagnets. Journal of Physics: Condensed Matter, 29(30):303001, 2017.

[23] ZQ Qiu and NV Smith. Quantum well states and oscillatory magnetic interlayer coupling. Journal of Physics: Condensed Matter, 14(8):R169, 2002.

[24] RA Duine, Kyung-Jin Lee, Stuart SP Parkin, and Mark D Stiles. Synthetic antiferromagnetic spintronics. Nature physics, 14(3):217–219, 2018.

doi:doi:10.6342/NTU202404801

[25] Ching-Hao Chang, Kun-Peng Dou, Guang-Yu Guo, and Chao-Cheng Kaun. Quantum-well-induced engineering of magnetocrystalline anisotropy in ferromagnetic films. NPG Asia Materials, 9(8):e424–e424, 2017.

[26] Ching-Hao Chang, Angus Huang, Sujit Das, Horng-Tay Jeng, Sanjeev Kumar, and R Ganesh. Carrier-driven coupling in ferromagnetic oxide heterostructures. Physical Review B, 96(18):184408, 2017.

[27] Juliana Lisik, Spencer Myrtle, and Erol Girt. Noncollinear interlayer exchange coupling across irfe spacer layers. Journal of Magnetism and Magnetic Materials, 585:171109, 2023.

[28] Zachary R Nunn, Claas Abert, Dieter Suess, and Erol Girt. Control of the noncollinear interlayer exchange coupling. Science Advances, 6(48):eabd8861, 2020.

[29] B Heinrich, JF Cochran, M Kowalewski, J Kirschner, Z Celinski, AS Arrott, and K Myrtle. Magnetic anisotropies and exchange coupling in ultrathin fcc co (001) structures. Physical Review B, 44(17):9348, 1991.

[30] M Rührig, R Schäfer, A Hubert, R Mosler, JA Wolf, S Demokritov, and P Grünberg. Domain observations on fe-cr-fe layered structures. evidence for a biquadratic coupling effect. physica status solidi (a), 125(2):635–656, 1991.

[31] A Azevedo, C Chesman, SM Rezende, FM De Aguiar, X Bian, and SSP Parkin. Biquadratic exchange coupling in sputtered (100) fe/cr/fe. Physical review letters, 76(25):4837, 1996.

[32] JC Slonczewski. Origin of biquadratic exchange in magnetic multilayers. Journal of Applied Physics, 73(10):5957–5962, 1993.

doi:doi:10.6342/NTU202404801

[33] SO Demokritov. Biquadratic interlayer coupling in layered magnetic systems. Journal of Physics D: Applied Physics, 31(8):925, 1998.

[34] Ching-Hao Chang and Tzay-Ming Hong. Interlayer coupling enhanced by the interface roughness: A perturbative method. Physical Review B, 79(5):054415, 2009.

[35] Y. Yafet. Ruderman-kittel-kasuya-yosida range function of a one-dimensional free-electron gas. Phys. Rev. B, 36:3948–3949, Sep 1987.

[36] R. Coehoorn. Period of oscillatory exchange interactions in co/cu and fe/cu multilayer systems. Phys. Rev. B, 44:9331–9337, Nov 1991.

[37] P. Bruno and C. Chappert. Oscillatory coupling between ferromagnetic layers separated by a nonmagnetic metal spacer. Phys. Rev. Lett., 67:1602–1605, Sep 1991.

[38] P. Bruno and Patrick Bruno. Theory of interlayer magnetic coupling. Physical Review B, 52(1):411–439, July 1995.

[39] Ching-Hao Chang, Kun-Peng Dou, Ying-Chin Chen, Tzay-Ming Hong, and Chao-Cheng Kaun. Engineering the interlayer exchange coupling in magnetic trilayers. Scientific reports, 5(1):16844, 2015.

[40] Patrick Bruno. Theory of interlayer exchange interactions in magnetic multilayers. Journal of Physics: Condensed Matter, 11(48):9403–9419, December 1999.

[41] Ching-Hao Chang and Tzay-Ming Hong. Switching off the magnetic exchange coupling by quantum resonances. Physical Review B, 85(21):214415, 2012.

[42] Koichi Momma and Fujio Izumi. VESTA 3 for three-dimensional visualization of crystal, volumetric and morphology data. Journal of Applied Crystallography, 44(6):1272–1276, December 2011.

doi:doi:10.6342/NTU202404801

[43] Georg Kresse and Jurgen Hafner. Norm-conserving and ultrasoft pseudopotentials for first-row and transition elements. Journal of Physics: Condensed Matter, 6(40):8245, 1994.

[44] Georg Kresse and Daniel Joubert. From ultrasoft pseudopotentials to the projector augmented-wave method. Physical Review B, 59(3):1758, 1999.

[45] Guan-Wei Peng, Hung-Chin Wang, Yu-Jie Zhong, Chao-Cheng Kaun, and Ching-Hao Chang. Driving noncollinear interlayer exchange coupling intrinsically in magnetic trilayers. Materials Today Physics, 48:101544, 2024.

[46] RK Kawakami, E Rotenberg, Ernesto J Escorcia-Aparicio, Hyuk J Choi, JH Wolfe, NV Smith, and ZQ Qiu. Determination of the magnetic coupling in the co/cu/co (100) system with momentum-resolved quantum well states. Physical review letters, 82(20):4098, 1999.

[47] Guan-Yu Chen, Angus Huang, Yen-Hui Lin, Chia-Ju Chen, Deng-Sung Lin, Po-Yao Chang, Horng-Tay Jeng, Gustav Bihlmayer, and Pin-Jui Hsu. Orbital-enhanced warping effect in px, p y-derived rashba spin splitting of monatomic bismuth surface alloy. npj Quantum Materials, 5(1):89, 2020.

[48] Y. Girard, C. Chacon, G. de Abreu, J. Lagoute, V. Repain, and S. Rousset. Growth of bi on cu(111): Alloying and dealloying transitions. Surface Science, 617:118–123, 2013.

[49] D. Kaminski, P. Poodt, E. Aret, N. Radenovic, and E. Vlieg. Surface alloys, overlayer and incommensurate structures of bi on cu(111). Surface Science, 575(3):233–246, 2005.

doi:doi:10.6342/NTU202404801

[50] J Henk, M Hoesch, J Osterwalder, A Ernst, and P Bruno. Spin–orbit coupling in the l-gap surface states of au(111): spin-resolved photoemission experiments and first-principles calculations. Journal of Physics: Condensed Matter, 16(43):7581, oct 2004.

[51] Sergiy Grytsyuk and Udo Schwingenschlögl. First-principles modeling of magnetic misfit interfaces. Phys. Rev. B, 88:165414, Oct 2013.

doi:doi:10.6342/NTU202404801